Myeloid *Slc2a1*-Deficient Murine Model Revealed Macrophage Activation and Metabolic Phenotype Are Fueled by GLUT1

Alex J. Freemerman,*[,1] Liyang Zhao,*[,1] Ajeeth K. Pingili,[†] Bin Teng,[†] Alyssa J. Cozzo,* Ashley M. Fuller,[‡] Amy R. Johnson,* J. Justin Milner,*[,2] Maili F. Lim,* Joseph A. Galanko,[§] Melinda A. Beck,* James E. Bear,[¶] Jeremy D. Rotty,[¶] Lavanya Bezavada,[∥] Heather S. Smallwood,[∥] Michelle A. Puchowicz,[∥] Juan Liu,[#] Jason W. Locasale,[#] Douglas P. Lee,** Brian J. Bennett,[††] E. Dale Abel,[‡‡,§§] Jeff C. Rathmell,[¶¶] and Liza Makowski*[,†]

Macrophages (MΦs) are heterogeneous and metabolically flexible, with metabolism strongly affecting immune activation. A classic response to proinflammatory activation is increased flux through glycolysis with a downregulation of oxidative metabolism, whereas alternative activation is primarily oxidative, which begs the question of whether targeting glucose metabolism is a viable approach to control MΦ activation. We created a murine model of myeloid-specific glucose transporter GLUT1 (*Slc2a1*) deletion. Bone marrow–derived MΦs (BMDM) from *Slc2a1*$^{M-/-}$ mice failed to uptake glucose and demonstrated reduced glycolysis and pentose phosphate pathway activity. Activated BMDMs displayed elevated metabolism of oleate and glutamine, yet maximal respiratory capacity was blunted in MΦ lacking GLUT1, demonstrating an incomplete metabolic reprogramming. *Slc2a1*$^{M-/-}$ BMDMs displayed a mixed inflammatory phenotype with reductions of the classically activated pro- and anti-inflammatory markers, yet less oxidative stress. *Slc2a1*$^{M-/-}$ BMDMs had reduced proinflammatory metabolites, whereas metabolites indicative of alternative activation—such as ornithine and polyamines—were greatly elevated in the absence of GLUT1. Adipose tissue MΦs of lean *Slc2a1*$^{M-/-}$ mice had increased alternative M2-like activation marker mannose receptor CD206, yet lack of GLUT1 was not a critical mediator in the development of obesity-associated metabolic dysregulation. However, *Ldlr*$^{-/-}$ mice lacking myeloid GLUT1 developed unstable atherosclerotic lesions. Defective phagocytic capacity in *Slc2a1*$^{M-/-}$ BMDMs may have contributed to unstable atheroma formation. Together, our findings suggest that although lack of GLUT1 blunted glycolysis and the pentose phosphate pathway, MΦ were metabolically flexible enough that inflammatory cytokine release was not dramatically regulated, yet phagocytic defects hindered MΦ function in chronic diseases. *The Journal of Immunology*, 2019, 202: 1265–1286.

M acrophages (MΦs) are a heterogeneous population of cells within the innate immune system that play critical roles in a myriad of processes, including development, tissue homeostasis, host defense, and tumor growth (1). MΦs exhibit a diverse spectrum of metabolic characteristics (2–10). In vitro studies have informed early findings that classically

*Department of Nutrition, University of North Carolina at Chapel Hill, Chapel Hill, NC 25799; [†]Department of Medicine, University of Tennessee Health Science Center, Memphis, TN 38163; [‡]Department of Medicine, University of North Carolina at Chapel Hill, Chapel Hill, NC 27599; [§]Department of Pathology and Laboratory Medicine, University of North Carolina at Chapel Hill, Chapel Hill, NC 27599; [¶]Department of Cell Biology and Physiology, University of North Carolina at Chapel Hill, Chapel Hill, NC 27599; [∥]Department of Pediatrics, University of Tennessee Health Science Center, Memphis, TN 38163; [#]Department of Pharmacology and Cancer Biology, Duke University School of Medicine, Duke University, Durham, NC 27710; **Omic Insight, Inc., Durham, NC 27713; [††]U.S. Department of Agriculture Western Human Nutrition Research Center, Davis, CA 95616; [‡‡]Division of Endocrinology and Metabolism, University of Iowa Carver College of Medicine, Iowa City, IA 52242; [§§]Fraternal Order of Eagles Diabetes Research Center, University of Iowa Carver College of Medicine, Iowa City, IA 52242; and [¶¶]Department of Pathology, Microbiology, and Immunology, Vanderbilt Center for Immunobiology, Vanderbilt University, Nashville, TN 37232

[1]A.J.F. and L.Z. are cofirst authors.

[2] Current address: Division of Biological Sciences, University of California, San Diego, La Jolla, CA.

ORCIDs: 0000-0003-1960-0199 (L.Z.); 0000-0002-0752-2130 (J.J.M.); 0000-0003-4871-6828 (M.A.B.); 0000-0002-7766-3502 (J.W.L.); 0000-0002-0766-3195 (B.J.B.); 0000-0001-5290-0738 (E.D.A.); 0000-0002-5337-8037 (L.M.).

Address correspondence and reprint requests to Dr. Liza Makowski, Cancer Research Building Room 322, Cancer Research Building, University of Tennessee Health Science Center, 19 South Manassas, Memphis, TN 38163. E-mail address: liza.makowski@uthsc.edu

The online version of this article contains supplemental material.

Abbreviations used in this article: *Arg1*, arginase 1; BMDM, bone marrow–derived MΦ; BMT, bone marrow transplant; CLS, crown-like structure; 2-DG, 2-deoxyglucose; ECAR, extracellular acidification rate; eWAT, epididymal white adipose tissue; FC, final concentration; GSH, glutathione; HFD, high-fat diet; iNOS, inducible NO synthase; LDL, low-density lipoprotein; *Ldlr*$^{-/-}$, lacking LDL receptor; LFD, low-fat diet; *LysMCre*, B6.129P2-*Lyz2*$^{tCAM(cre)Ifo}$/J; *Lyz2*, lysozyme 2; MΦ, macrophage; MFI, median fluorescence intensity; MID, mass isotopomer distribution; MOMA2, MΦ/monocyte mAb; MRI, magnetic resonance imaging; OCR, oxygen consumption rate; ORO, Oil Red O; PAI-1, plasminogen activator inhibitor-1; PPP, pentose phosphate pathway; qPCR, quantitative PCR; ROS, reactive oxygen species; SVF, stromal-vascular fraction; UNC, University of North Carolina.

activated ("M1"-like) MΦs use primarily glycolysis, which is linked to the proinflammatory phenotype characterized by the production of high levels of proinflammatory cytokines and reactive oxygen and nitrogen metabolites plus microbicidal and phagocytic properties (11–13). In contrast, alternatively activated ("M2"-like) MΦs predominantly rely on mitochondrial oxidative metabolism (13–20), with a lesser dependence on glycolysis (21–24). Alternative M2-like MΦs are associated with tissue homeostasis and resolution of the inflammatory response. Yet recent in vivo and in vitro studies underscore that classical and alternative phenotypes are not dichotomous but overlap (25, 26). Importantly, immunometabolism has emerged as a critical driver of MΦ activation and phenotype (26); however, minimal research has been conducted to understand how the metabolic phenotype of MΦs influences disease progression (3, 27). Thus, a better understanding of MΦ metabolism may shed an innovative light on the pathological basis of disease and lead to the future development of MΦ-targeted treatment approaches.

We have previously reported that the glucose transporter GLUT1 (encoded by *Slc2a1*) is a critical modulator of MΦ glucose metabolism and inflammation (11). Overexpression of GLUT1 in MΦs significantly increased glucose uptake, glycolysis, and the expression of proinflammatory cytokines associated with systemic metabolic dysfunction (e.g., TNF-α, IL-1β, and IL-6) even in the absence of activating stimuli. Expression of plasminogen activator inhibitor-1 (PAI-1), a GLUT1-dependent cytokine associated with metabolic disease, was also increased in a glycolysis- and reactive oxygen species (ROS)–dependent manner (11, 27). Furthermore, GLUT1 expression was identified in adipose tissue crown-like structures (CLS), aggregates of immune cells surrounding dead or dying adipocytes that are increased in adipose tissue of obese mice and humans (11). Flow cytometric analysis revealed that adipose tissue MΦs that highly expressed GLUT1 also had greater TNF-α expression (11). Taken together, these results implicated GLUT1 as a critical modulator of MΦ metabolism and inflammatory capacity, suggesting that GLUT1 or glycolysis could be an attractive target to limit inflammation, but loss of function studies were lacking.

Because GLUT1 is the primary receptor for glucose uptake in MΦs (11), we hypothesized that restricting glucose uptake through GLUT1 ablation could impact metabolic and immunoregulatory pathways. In this article, we report that bone marrow–derived MΦs (BMDMs) lacking GLUT1 (*Slc2a1*$^{M-/-}$) demonstrated a reduced inflammatory phenotype with evidence of substrate switch, resorting to elevated fatty acid and glutamine metabolism in the absence of GLUT1-mediated glycolysis and pentose phosphate pathway (PPP). In addition, *Slc2a1*$^{M-/-}$ BMDMs displayed reduced oxidative stress and increased capacity to buffer from oxidative insult. Taken together, the absence of GLUT1 limited overall activation with a potentially more alternatively activated phenotype. Because of this complex phenotype, we hypothesized that the absence of GLUT1-mediated metabolism in MΦs may protect against pathogenic sequelae of diseases associated with MΦ inflammation.

We next examined the effects of myeloid-specific *Slc2a1* deletion in two models of MΦ-associated disease: diet-induced obesity and atherosclerosis. As adipose tissue expands in obesity, MΦ content increases considerably, where they play a role in cell turnover, lipid trafficking, and inflammation and subsequent metabolic dysfunction (9, 20, 28–31). Thus, we hypothesized that deleting GLUT1 in MΦs would reduce obesity-associated adipose tissue inflammation and thereby modulate the onset of metabolic dysfunction. Unexpectedly, in adipose tissue of obese *Slc2a1*$^{M-/-}$ animals, we observed an elevation in markers of MΦ infiltration and increased expression of proinflammatory mediators such as MCP-1 (*Ccl2*) compared with obese control mice. However, despite increased MΦ infiltration in

obese *Slc2a1*$^{M-/-}$ adipose tissue, there were no differences in glucose or insulin tolerance between *Slc2a1*$^{M-/-}$ mice and obese floxed littermate controls, measures typically associated with MΦ markers, thus indicating that increased MΦ infiltration failed to elicit a commensurate increase in the typical proinflammatory response in the absence of GLUT1. Interestingly, in older mice, flow cytometric analysis of adipose tissue MΦs from lean *Slc2a1*$^{M-/-}$ mice revealed increased expression of mannose receptor CD206, an alternative M2-like marker. Thus, despite skewing of the MΦ phenotype toward the alternative phenotype, deficiency of myeloid GLUT1 surprisingly did not alter diet-induced obesity-associated systemic pathological conditions. MΦs also play a critical role in the pathogenesis of atherosclerosis through clearance of modified low-density lipoprotein (LDL) particles, efferocytosis, and control of the immune milieu (32, 33). Therefore, we next determined whether lack of GLUT1-mediated glucose metabolism in MΦs would reduce the extent of atherogenesis. In *Slc2a1*$^{M-/-}$ bone marrow–recipient *Ldlr*$^{-/-}$ mice (*Slc2a1*$^{M-/-}$ *Ldlr*$^{-/-}$), a greater percentage of mice suffered from large, necrotic, and unstable lesions compared with *Slc2a1*$^{fl/fl}$ recipient mice (*Slc2a1*$^{fl/fl}$ *Ldlr*$^{-/-}$), despite a lack of major systemic alterations. Interestingly, further analyses demonstrated significantly impaired phagocytic capacity in *Slc2a1*$^{M-/-}$ MΦs, which may have contributed to defective tissue homeostasis in lesions. Together, these studies illuminate a critical role for myeloid-specific GLUT1-mediated glucose metabolism in directing inflammatory potential of MΦs.

Materials and Methods
Reagents

All reagents were obtained from Sigma-Aldrich (St. Louis, MO) unless otherwise noted. IFN-γ and IL-4 were obtained from R&D Systems (Minneapolis, MN). M-CSF was obtained from BioLegend (San Diego, CA). LPS (*E. coli* L4391; Sigma-Aldrich) was diluted in sterile PBS at a final concentration of 1 mg/ml. Novolin human insulin was purchased from Novo Nordisk (Plainsboro, NJ). Glucometer and glucose strips were purchased from Abbott Diabetes Care (Abbott Park, IL). FBS, RPMI 1640, 100× L-glutamine, and 100× penicillin/streptomycin antibiotic mix were obtained from CellGro (Corning, NY). Abs were purchased from the following sources: anti-F4/80 (MCA497) and MΦ/monocyte mAb (MOMA2) (MCA519G) (AbD Serotec/Bio-Rad, Hercules, CA), anti-GLUT1 (ab40084; Abcam, Cambridge, MA), anti-actin (MAB1501) (EMD Millipore, Billerica, MA), and Annexin V Apoptosis Detection Kit PE (Thermo Fisher Scientific, Waltham, MA); mouse IgG (Thermo Fisher Scientific); goat anti-mouse IgG, Rhodamine Red conjugate (Thermo Fisher Scientific); goat anti-mouse IgG Cy5 (Thermo Fisher Scientific); and Alexa Fluor 488 Phalloidin (Thermo Fisher Scientific) or peroxidase-conjugated goat anti-mouse secondary Ab (NXA931; GE Healthcare Life Science, Piscataway, NJ). Fluoro-Gel II with DAPI was purchased from Electron Microscopy Sciences (Hatfield, PA). Carboxylate microspheres were obtained from Polysciences (Warrington, PA).

Animals and maintenance

Animal studies were performed with approval and in accordance with the guidelines of the Institutional Animal Care and Use Committee at the University of North Carolina (UNC) at Chapel Hill and University of Tennessee Health Science Center. All animals were housed in a temperature-controlled facility with a 12-h light/dark cycle and ad libitium access to food and water. B6.129P2-*Lyz2*$^{tCAM(cre)Ifo}$/J (*LysMCre*) mice (stock number: 004781), *Ldlr*$^{-/-}$ mice (stock number: 002207), and C57BL/6J mice (stock number: 000664) were purchased from The Jackson Laboratory (Bar Harbor, ME). Floxed *Glut1* mice on a C57BL/6J background were a kind gift from E.D. Abel (34) (University of Iowa). For experiments, control mice had two floxed *Glut1* alleles and no LysMCre alleles (*Slc2a1*$^{fl/fl}$), whereas myeloid-specific *Slc2a1* knockouts harbored two floxed alleles and one LysMCre allele (*Slc2a1*$^{M-/-}$) as shown in Fig. 1A.

DNA isolation and genotyping

Genomic DNA was isolated from tail biopsies using a DNeasy Blood and Tissue Kit (Qiagen, Valencia, CA). Genotyping for *LysMCre* is detailed on

The Jackson Laboratory's Web site (http://jaxmice.jax.org). Genotyping for *Glut1* was performed using the following primers: flanked loxP forward – 5′-CTGTGAGTTCCTGAGACCCTG-3′; flanked loxP reverse – 5′-CCCAGGCAAGGAAGTAGTTC-3′. The primers flank the upstream LoxP site located upstream of exon 3. The resulting PCR products are either only wild-type DNA (product ≈350 bp) or wild-type DNA with the upstream LoxP site included (floxed product ≈500 bp). The following amplification scheme was used: 98°C for 1 min for 1 cycle; 98°C for 10 s, 58°C for 10 s, 98°C for 25 s for 40 cycles; and then 4°C to soak. iProof High-Fidelity PCR supermix (Bio-Rad)–based genotyping was performed on a C1000 Touch Thermal Cycler (Bio-Rad).

Hematologic analysis

Hematologic analysis was conducted on fed 8-wk-old *Slc2a1^{fl/fl}* and *Slc2a1^{M−/−}* age-matched male mice maintained on ad libitum chow. Flow cytometry was used to enumerate circulating leukocyte populations. Blood was collected, and RBCs were lysed in ACK lysis buffer. Cells were washed twice in HBSS, resuspended in PBS, counted, and then 1×10^5 cells were stained with CD45-FITC, F4/80-PE, Ly6G/C-PE-Cy7, CD11b-allophycocyanin, and CD11c-allophycocyanin-eFluor 780 in the presence of anti-CD16/32 (Fc block) in FACS buffer (1% FBS in PBS) as described by Johnson et al. (20). Samples were analyzed on the Dako CyAn ADP flow cytometer (Beckman Coulter, Fullerton, CA) and FlowJo Software (TreeStar, Ashland, OR).

Cell culture and primary cell isolation

To generate BMDM, bone marrow was harvested from age-matched male *Slc2a1^{fl/fl}* and *Slc2a1^{M−/−}* as previously described (20). BMDMs were generated by culturing marrow cells in 10-cm non–tissue culture–treated dishes for 6 d with 20 ng/ml M-CSF or 30% L929 conditioned media supplemented as indicated, in RPMI 1640 supplemented with 10% FBS, $1\times$ L-glutamine, and $1\times$ penicillin/streptomycin antibiotic mix. BMDMs were left untreated as naive, unstimulated MΦs or activated using 5 ng/ml LPS and 10 ng/ml IFN-γ (M1-like) or 10 ng/ml IL-4 (M2-like) for 24 h (11, 13, 20). Cell densities and viability were determined by hematocytometer and trypan blue exclusion, respectively. Cell size, volume, and viability were determined using a Sceptor handheld automated cell counter (Millipore). To isolate peritoneal MΦs, mice were injected i.p. with 1 ml of sterile 4% thioglycollate. Four days later, thioglycollate-elicited peritoneal MΦs were obtained as described (35). All cultures were maintained under a fully humidified atmosphere of 95% air and 5% CO_2 at 37°C.

Substrate metabolism and metabolomics

Slc2a1^{fl/fl} versus *Slc2a1^{M−/−}* BMDMs were plated at 4.0×10^5 cells per well into 24-well plates and allowed to attach overnight. Cells were activated as described above, and uptake and metabolism of substrates were measured as in Freemerman et al. (11). Briefly, [³H]-glucose uptake was measured for 10 min at 37°C in 0.5 ml/well KRH buffer (136 mM NaCl, 4.7 mM KCl, 1.25 mM CaCl₂, 1.25 mM MgSO₄, 10 mM HEPES [pH 7.4]) with 0.5 μCi/ml [³H]2-Deoxy-D-glucose (PerkinElmer, Waltham, MA). Glucose oxidation to CO_2 was measured by incubating cells with ubiquitously labeled [¹⁴C]-glucose for 2 h and then measuring [¹⁴C]-CO_2 in the media (36). Oleate oxidation to CO_2 was measured by incubating cells with 1-[¹⁴C]-oleate for 2 h and measuring [¹⁴C]-CO_2 in the media. Protein concentrations were determined with a BCA assay (Thermo Fisher Scientific). BODIPY-palmitate uptake was measured by flow cytometry to quantitate fatty acid uptake. For targeted metabolomics analysis, *Slc2a1^{fl/fl}* or *Slc2a1^{M−/−}* were plated on 10-cm non–tissue culture–treated dishes at 5×10^5 cells/ml and allowed to attach overnight. Fresh media was added, and cells were left as unstimulated or LPS/IFN-γ–activated for 24 h. PBS-washed cells were detached by trypsin and pelleted for analysis by Metabolon (Durham, NC) (11, 37), with *n* = 4 replicates per group. Data are presented as relative measures of "scaled intensity" after normalization to protein and median scaling to 1. Missing values were imputed with the minimum. The principal component analysis plot was constructed using ArrayStudio V5.0 (OmicSoft, Cary, NC).

Cellular bioenergetics analyses

Metabolic phenotyping assays were conducted on *Slc2a1^{fl/fl}* versus *Slc2a1^{M−/−}* BMDMs (11, 38). Seahorse glycolysis and mitochondrial stress tests were conducted on the Seahorse Bioscience XF96 Extracellular Flux Analyzer (Billerica, MA) after optimization. Four doses of cell densities, concentrations of FCCP, and concentrations of oligomycin were tested in both stress tests for the best metabolic performance of BMDMs. For all assays, 50,000 BMDMs was determined to be the best concentration along with 1.5 μM FCCP or 1 μM oligo. BMDMs were seeded in a

Seahorse Bioscience (Billerica, MA) 96-well plate in RPMI 1640 supplemented with 20 ng/ml M-CSF and incubated overnight at 37°C in an atmosphere of 5% CO_2. Cells were left unstimulated or LPS/IFN-γ– or IL-4–stimulated for 24 h. Glycolysis stress test assay medium included XF Base Media (DMEM) purchased from Seahorse with 2 mM glutamine supplemented. Glucose was injected to a final concentration (FC) of 10.0 mM, oligomycin to an FC of 1.0 μM, and 2-deoxyglucose (2-DG) to an FC of 50 mM. For the mitochondrial stress test, medium included XF Base Media (DMEM) with 10 mM glucose, 2 mM glutamine, and 1 mM sodium pyruvate supplemented. In the mitochondrial stress test, oligomycin was injected to an FC of 1.0 μM, FCCP to an FC of 1.5 μM, and rotenone/antimycin A (Sigma-Aldrich) to an FC of 0.50 μM. All reagents were sterile, and all experimental media were freshly prepared and at a pH of 7.4 before each assay. Live and dead cell analysis using calcein AM and EthD-1, respectively, did not reveal any change in death or number of live cells by treatment or genotype (Molecular Probes, Eugene, OR, data not shown). Bioenergetics were determined by recording extracellular acidification rates (ECAR; milli-pH units per minute) and oxygen consumption rates (OCR; picomol of O_2 per minute). All rates were normalized to DNA content using CyQUANT Cell Proliferation Assay Kit (Molecular Probes) and quantified on CLARIOstar BMG Lab Tech (Cary, NC).

[¹³C]-glutamine enrichment, extraction, and liquid chromatography–mass spectrometry analysis

BMDM were differentiated from bone marrow of age-matched 10-wk-old male control and *Slc2a1^{M−/−}* littermates and plated onto six-well plates. The next day, cells were stimulated with LPS/IFN-γ for 24 h as described above. Cells were plated with unlabeled 4 mM [¹²C]-glutamine growth media (*n* = 2 per genotype) and were used to calculate natural abundance (background) of each metabolite measured. For experimental cells, [¹²C]-glutamine was replaced with sterile 4 mM [U-¹³C]-glutamine (Isotec/Millipore) in the same conditions, except for phenol red–free RPMI for the last 16 h of LPS/IFN-γ stimulation. Media was removed from cells, and 1 ml of ice-cold 80% methanol was added to each well on dry ice. Plates were placed in −80°C for 15 min to inactivate enzymatic activity. Scraped lysates were collected into Eppendorf tubes and dried in a vacuum concentrator at room temperature. Metabolite extraction was performed as described in our previous study (39). The dry pellets were reconstituted into 30 μl of sample solvent (water/methanol/acetonitrile, 2:1:1, v/v), and 3 μl was analyzed by liquid chromatography–mass spectrometry for mass isotopomer distribution (MID) of each metabolite. Ultimate 3000 UHPLC (Dionex) was coupled to Q Exactive Plus-Mass spectrometer (Thermo Scientific) for metabolite profiling. A hydrophilic interaction chromatography method employing an Xbridge amide column (100 × 2.1 mm inner diameter, 3.5 μm; Waters) is used for polar metabolite separation. A detailed liquid chromatography method was described previously (40), except that mobile phase A was replaced with water containing 5 mM ammonium acetate (pH 6.8). The Q Exactive Plus-Mass spectrometer is equipped with a HESI Probe with related parameters set as below: heater temperature, 120°C; sheath gas, 30; auxiliary gas, 10; sweep gas, 3; spray voltage, 3.0 kV for the positive mode and 2.5 kV for the negative mode; capillary temperature, 320°C; S-lens, 55; and a mass to charge ratio of 70 to 900 was used in positive mode from 1.31 to 12.5 min. For negative mode, the parameters were as follows: a scan range of 70–900 was used from 1.31 to 6.6 min and then 100 to 1000 was used from 6.61 to 12.5 min; resolution: 70,000; and automated gain control, 3×10^6 ions. Customized mass calibration was performed before data acquisition. Liquid chromatography–mass spectrometry peak extraction and integration were performed using commercially available software Sieve 2.2 (Thermo Fisher Scientific). The peak area was used to represent the relative abundance of each metabolite in different samples. The missing values were handled as described in our previous study (40). The fractional contribution of [¹³C]-glutamine to each of the metabolite pools was determined from the molar percent enrichments as calculated from the MIDs after correction for natural abundance. Two-way ANOVA with Tukey correction was used to test for genotype effect in each isotope.

Quantitative RT-PCR analysis

mRNA was isolated using Qiagen's RNeasy mini kit. The RNA quantity and quality were determined using Nanodrop (Thermo Fisher Scientific) and reverse transcribed into cDNA using the iScript cDNA synthesis kit (Bio-Rad). The expression of specific genes was quantitated by quantitative PCR (qPCR) using Assay-On-Demand (Thermo Fisher Scientific) or Roche's Universal ProbeLibrary (Indianapolis, IN) on an ABI 7900HT machine (Thermo Fisher Scientific) as in Qin et al. (41). Expression levels of genes of interest were normalized to expression of the rRNA

18S. Animals whose body weight was at or above the mean body weight for the high-fat diet (HFD) and low-fat diet (LFD) experimental groups were selected for analysis; therefore, unless indicated, $n = 8–9$ per group for mouse data and $n = 3–6$ experiments for BMDM studies. Data are presented as $^{\Delta\Delta}$Ct calculations normalized to the baseline value.

Microarray analysis

RNA sample quality was assessed using the RNA ScreenTape assay (Agilent, Santa Clara, CA). Samples (2 μl) were Cy3-labeled with the Agilent Low-Input Quick Amp Labeling Kit and hybridized to SurePrint G3 Mouse GE 8 × 60K microarrays (Agilent). Four biological replicates for each of three BMDM activation states (unstimulated, LPS/IFN-γ, and IL4) from both *Slc2a1*$^{M−/−}$ and *Slc2a1*$^{fl/fl}$ mice were measured (National Center for Biotechnology Information Gene Expression Omnibus upload; accession number: GSE123289; https://www.ncbi.nlm.nih.gov/geo/query/acc.cgi?acc=GSE123289). Hierarchical gene clustering was conducted using the average linkage clustering algorithm in Cluster 3.0 (Stanford, CA). Two-class unpaired significance of microarray analyses were then performed. Normalized data from *Slc2a1*$^{M−/−}$ BMDMs were log transformed using Cluster 3.0, and genes were again clustered hierarchically using an average linkage algorithm. Heat maps were generated using Java TreeView. Data are presented as the log2-based fold change of each gene in individual *Slc2a1*$^{M−/−}$ samples relative to the average expression of that gene across all four *Slc2a1*$^{fl/fl}$ samples. Ingenuity Pathway Analysis (Redwood City, CA) was used to identify significant functions and pathways ($p < 0.05$ with Benjamini–Hochberg correction for multiple comparisons testing). Metaboanalyst was used to integrate metabolite and gene expression data for pathway analysis, according to default parameters.

Protein expression analysis

Cells were lysed in radioimmunoprecipitation assay buffer (50 mM Tris, 150 mM NaCl, 0.1% SDS, 0.5% deoxycholate, 1% TX-100) with 1× protease and phosphatase inhibitors (Sigma-Aldrich). Protein concentration was determined using the BCA assay (Thermo Fisher Scientific). Anti-GLUT1 primary Ab, anti-actin Ab, or peroxidase-conjugated goat anti-mouse secondary Ab (NXA931; GE Healthcare Life Science, Piscataway, NJ) were used and developed by chemiluminescence (Amersham ECL Select; GE Healthcare Life Science) and quantitated using a VersaDoc 4000 instrument and software (Bio-Rad) or Li-Cor Odyssey (Lincoln, NE). Blots were quantitated from three separate experiments. All lanes were normalized to β-actin for loading. Concentrations of IL-6, TNF-α, IL1β, IL-10, and MCP-1 in conditioned media were measured using a MAGPIX Luminex kit (EMD Millipore).

Atherosclerosis study: bone marrow transplantation and metabolic parameters

The atherosclerosis study was conducted as previously described (42). Briefly, at 6 wk of age, *Ldlr*$^{−/−}$ mice received two doses of x-ray radiation (500 cGy × 2, spaced 4 h apart; X-RAD, North Branford, CT) and were then transplanted with bone marrows isolated from *Slc2a1*$^{fl/fl}$ or *Slc2a1*$^{M−/−}$ donor mice. Control animals were transplanted with the HBSS buffer only and died within 10–11 d of lethal irradiation. Following bone marrow transplant (BMT) (43), chimeric *Ldlr*$^{−/−}$ mice were transferred to sterile cages with ad libitium access to sterile mouse chow and sterile water and were maintained on a chow diet for 4 wk before challenge with Western diet (TD88137, 42% of Kcal from milk fat with 0.15% added cholesterol) from Harlan Teklad (Indianapolis, IN) for 12 wk. Body weight and body composition was measured daily by magnetic resonance imaging [MRI] across the study. Fasting plasma lipids were measured in the UNC Animal Clinical Chemistry and Gene Expression Core Facility. Blood pressure was measured using a tail-cuff system in UNC Rodent Advanced Surgical Models Core Lab of the UNC McAllister Heart Institute. Mice ($n = 8$) received five consecutive days of training on the tail-cuff blood pressure system (CODA; Kent Scientific, CA) prior to data collection. Starting on day 6, systolic and diastolic blood pressure was measured in conscious mice daily for 3 d. Mice were acclimated to the warm (32°C) restrainer for 15 min and blood pressure was recorded during 10 acclimations followed by 25 measurement cycles.

Aortic histology and immunohistochemistry quantification

Mice dissections were done as previously described (42). Briefly, following dissection, hearts were either transferred to 70% ethanol and stored at 4°C for future creation of formalin-fixed, paraffin-embedded sections or transferred to 30% sterile sucrose for 72 h for generating cryosectioning slides. Formalin-fixed, paraffin-embedded sections were stained with Masson's trichrome for quantification of collagen content, necrotic core areas, and subendothelium cell numbers, and with anti-MOMA2 for MΦs. Frozen sections were stained with Oil Red O (ORO) for quantification of lesion area. A color deconvolution algorithm, developed by UNC Translational Pathology Laboratory, was used for digital quantification of collagen, reported as OD × percent of total positive area stained with collagen (44–46). Necrotic core size and subendothelial cell nuclei were quantified on Masson's trichrome–stained slides, which were normalized to the total quantified area. Necrotic core size was measured using Aperio ePathology software (Aperio, Buffalo Grove, IL), and subendothelial cell numbers were assessed manually by counting nuclei. Quantification of MΦs was calculated as OD × percent of total positive area stained with anti-MOMA2. Quantification of atherosclerotic lesions was done as described with modification (47, 48).

Obesity study: metabolic phenotyping

Mice were weaned onto and given ad libitum access to either a purified diet containing 10% kCal from fat (LFD; D12450B; Research Diets, New Brunswick, NJ) or a diet containing 45% kCal from fat (HFD; D12451; Research Diets) for 23 wk ($n = 14–19$ mice per diet per genotype). Body weight was measured prior to starting mice on LFD or HFD at weaning and weekly thereafter. Body composition was measured at 4, 8, and 20 wk using the EchoMRI-100 quantitative magnetic resonance whole body composition analyzer (EchoMRI Medical Systems, Houston, TX). Blood glucose was measured at 3 wk on the diets and again at termination, both following a 6-h fast. i.p. glucose tolerance tests and insulin tolerance tests were performed at weeks 21 and 22 on diet, following 6- and 4-h fast, respectively (42). Briefly, 2.0 gm/kg body weight of glucose or 0.75 U of insulin was injected i.p., and blood glucose was measured over 120 min. Plasma insulin was measured by ELISA (EMD Millipore). Energy expenditure was evaluated in TSE Systems cages over 48 h on a subgroup of mice at 23 wk ($n = 3–5$ per group).

Epididymal white adipose tissue and blood collection

For tissue collection, blood was collected via cardiac puncture from anesthetized mice. Plasma was separated from other blood components by centrifugation at 200 × g for 5 min at 4°C. Epididymal white adipose tissue (eWAT) was collected and fixed in 10% formalin for histological analyses. A portion of each tissue was flash frozen in liquid nitrogen. Anti-F4/80 immunohistochemical staining was conducted, as previously described (46). All histological sections were analyzed using ScanScope Image Analysis Toolbox software (Buffalo Grove, IL) (46). CLS were quantitated under original magnification ×20 by counting six identically sized boxed areas (fields) placed randomly over the scanned area of interest. CLS are presented as CLS per field.

Flow cytometric analysis of epididymal white adipose MΦs

Male *Slc2a1*$^{fl/fl}$ and *Slc2a1*$^{M−/−}$ mice ($n = 4$ per diet and genotype) were weaned onto a LFD or HFD at 3 wk of age and maintained on diets for an average of 46.14 wk. Mice were anesthetized by i.p. injection of 2,2,2-tribromoethanol in tertiary amyl alcohol (250 mg/kg), followed by exsanguination via cardiac puncture and subsequent cervical dislocation. The peri-epididymal adipose pad from each mouse was excised and transferred to ice-cold high-glucose DMEM (Corning, Corning, NY) containing 20 mM HEPES buffer (Cellgro, Manassas, VA), 10% bovine calf serum (Hyclone, GE Healthcare Life Sciences, South Logan, UT), 10% glutamine, and 10% penicillin-streptomycin. Individual adipose pads were weighed, imaged, and minced with surgical scissors. A single-cell suspension was generated by digestion in 2 mg/ml type I collagenase (Worthington, Lakewood, NJ) at 37°C followed by gentle mechanical dissociation using a Stomacher 80 Biomaster small tissue laboratory paddle blender (Seward, Worthing, West Sussex, U.K.). An immune cell–enriched stromal-vascular fraction (SVF) was obtained by dilution with an equal volume of HEPES-buffered DMEM, filtration through a 100-μm cell strainer, and centrifugation at 200 × g for 10 min at 4°C. The resulting SVF pellet was incubated in ACK lysis buffer (Life Technologies, Gaithersburg, MD) for 3–5 min at room temperature to lyse RBCs and then washed in HEPES-buffered DMEM. A 10-μl aliquot of cell suspension was diluted 1:2 with trypan blue, followed by analysis of live cells using a Bio-Rad TC 20 automated cell counter to determine total SVF cells obtained from adipose pads of individual mice. Two million SVF cells per mouse were transferred to a 96-well plate, blocked, and stained with pretitrated Abs. Abs or stains were used as follows: 1) Fc block (CD16/32) at 1:50 (no. 101320, lot B200134; BioLegend), 2) live/dead (Zombie Green) at 1:400 (no. 423111; BioLegend), 3) CD45 (BV605) at 1:200 (no. 103140, lot B211813; BioLegend), 4) CD11b (BUV395) at 1:100 (no. 563553, lot 6028814; BD Biosciences), 5) CD64 (PE-Cy7) at 1:200 (no. 139313, lot B197402; BioLegend), and 6) CD206 (BV785) at 1:100 (no. 141729, lot B229782; BioLegend). The remaining

SVF cells from each adipose pad were pooled for single-color and fluorescence-minus-one controls. Live–dead discrimination was conducted using Zombie Green fixable viability dye (BioLegend), according to manufacturer instructions. Abs for extracellular Ag staining were diluted in Dulbecco's PBS containing 2% FBS and 5 mM EDTA. SVF cells were then washed twice, fixed/permeabilized using Cytofix/Cytoperm Fixation/Permeabilization solution (BD Biosciences, San Jose, CA), and resuspended in Dulbecco's PBS containing 2% FBS and 5 mM EDTA. Following filtration through a 30-μm filter, SVF cells were analyzed on a BD LSR II flow cytometer. Compensation was set using single-stained cellular controls, and gating was determined based on fluorescence-minus-one controls. Data were analyzed with FlowJo software, version 10 (FlowJo, Ashland, OR).

Microsphere engulfment phagocytic assay

Using carboxylate microspheres, phagocytic capacity in thioglycollate-elicited peritoneal MΦs was measured ex vivo (42, 49). Briefly, thioglycollate-elicited peritoneal MΦs were seeded on collagen-coated Nunc Lab-Tek Chamber Slides (Sigma-Aldrich) overnight. The next day, carboxylated microspheres were incubated with MΦs for either 20 or 60 min at 37°C. Goat anti-mouse Rhodamine Red-X (Life Technologies, CA) was first incubated with cells for 15 min. Cells were then permeabilized. Goat anti-mouse Cy5 and Alexa 488-Phalloidin (Life Technologies) were then incubated with cells for another 30 min. Cells were then mounted with fluorescent mounting media. A ZEISS LSM 700 confocal microscope was used to capture the images (UNC Microscopy Core). Phagocytosis index was calculated by numbers of microspheres adherent to or engulfed by cells, respectively, divided by total nuclei in the field and reported as beads per cell. Experiments were repeated three times, with four technical replicates per genotype per experiment, and two fields per well from each experiment were captured for analysis.

ROS production

$Slc2a1^{fl/fl}$ or $Slc2a1^{M-/-}$ BMDMs were either untreated or stimulated with LPS 100 ng/ml for 4 h. Cells were incubated with dihydroxyrhodamine (DHR-1,2,3; Sigma-Aldrich) for 20 min and then trypsinized for flow cytometric analysis. Total ROS was quantified using a Beckman Coulter CyAn ADP flow cytometer (Brea, CA). Flow cytometry data were analyzed using FlowJo software (TreeStar), and median fluorescence intensity (MFI) was quantified in at least 5×10^3 cellular events.

Statistics

For all in vivo and ex vivo data, statistical differences between experimental groups were determined by two-way ANOVA, and Tukey correction for multiple comparisons were performed using statistical software within GraphPad Prism, as indicated (GraphPad Software, La Jolla, CA). For body weight data, to account for the repeated measures over time within animals, an autoregressive within-subject correlation matrix was fit. F-tests using the resulting parameter and SE estimates were constructed to make comparisons of interest. Analyses were performed using SAS Version 9.3 (SAS Institute, Cary, NC). All experiments were repeated three or more times in triplicate, unless otherwise indicated. Data are shown as mean ± SEM. The p values < 0.05 were considered statistically significant.

Results

Lack of GLUT1 impaired glucose uptake and oxidation, leading to a substrate switch in MΦs

As shown in Fig. 1A, $Slc2a1^{fl/fl}/LysMCre^{+/-}$ mice were bred to generate male $Slc2a1^{M-/-}$ mice (two floxed $Slc2a1$ alleles and two $LysMCre$ alleles) and littermate $Slc2a1^{fl/fl}$ controls (two floxed $Slc2a1$ alleles and no LysMCre alleles). We first investigated whether $Slc2a1$ deletion reduced the number of circulating myeloid cells, such as neutrophils and cells of the monocyte-MΦ lineage. Using flow cytometry, hematologic analyses did not show any significant differences in circulating myeloid cells in $Slc2a1^{M-/-}$ mice compared with $Slc2a1^{fl/fl}$ mice, confirming that $Slc2a1$ deletion did not impair differentiation of select myeloid lineages or their egress from bone marrow [data not shown; gating strategy is the same as our previous work (20)]. Differentiated BMDMs from $Slc2a1^{M-/-}$ mice were viable with no apparent morphological differences from $Slc2a1^{fl/fl}$ BMDMs (data not shown). To determine the impact of $Slc2a1$ deletion on MΦ activation, BMDMs were either left unstimulated or

treated with 5 ng/ml LPS and 10 ng/ml IFN-γ or 10 ng/ml IL-4 for 24 h to model classical/M1-like or alternative/M2 activation, respectively (11, 13). Lack of $Slc2a1$ mRNA and GLUT1 protein was confirmed in unstimulated, LPS/IFN-γ–, and IL4-activated BMDMs, indicating successful ablation through LysMCre recombinase activity (Fig. 1B, 1C, $p < 0.0001$ $Slc2a1^{fl/fl}$ versus $Slc2a1^{M-/-}$). We next determined the dependence of MΦ metabolic phenotype upon GLUT1-mediated glucose transport by assessing glucose uptake, glucose oxidation, fatty acid uptake, and fatty acid oxidation. Uptake of ^{3}H–2-DG in control $Slc2a1^{fl/fl}$ LPS/IFN-γ–activated BMDMs was significantly increased by 26-fold relative to unstimulated $Slc2a1^{fl/fl}$ BMDMs (Fig. 1D, $p < 0.0001$ control cells, black bars, unstimulated versus LPS/IFN-γ) (11). However, in the absence of GLUT1, 2-DG uptake was essentially abolished in $Slc2a1^{M-/-}$ BMDMs in both unstimulated and IL4-stimulated MΦs, whereas glucose uptake was dramatically reduced in $Slc2a1^{M-/-}$ LPS/IFN-γ–stimulated MΦs compared with $Slc2a1^{fl/fl}$ controls (Fig. 1D, $p < 0.0001$ $Slc2a1^{fl/fl}$ versus $Slc2a1^{M-/-}$). The slight increase in glucose uptake in LPS/IFN-γ–stimulated MΦs may be due to contaminating cells in the BMDM preparation. We determined that preparations were 97.7% MΦs (data not shown). Indeed, in a more pure population of MΦs, glucose uptake was similarly ablated in $Slc2a1^{M-/-}$ thioglycollate-elicited peritoneal MΦs compared with $Slc2a1^{fl/fl}$ controls, both at baseline and following stimulation with LPS (Fig. 1E, $p < 0.0001$ $Slc2a1^{fl/fl}$ versus $Slc2a1^{M-/-}$). Radiotracer studies demonstrated that glucose oxidation was increased in floxed controls in LPS/IFN-γ–activated BMDM by 1.7-fold, likely because of the increased glucose flux through the PPP and tricarboxylic acid cycle associated with proinflammatory activation (Fig. 1F). However, glucose oxidation was decreased by 65–90% in $Slc2a1^{M-/-}$ BMDMs in the unstimulated, LPS/IFN-γ, and IL4 treatments compared with $Slc2a1^{fl/fl}$ BMDMs (Fig. 1F; $p < 0.0001$ $Slc2a1^{fl/fl}$ versus $Slc2a1^{M-/-}$). To determine if the absence of GLUT1-mediated glucose entry also altered fatty acid use, we used fluorescent and radiotracer studies to measure fatty acid uptake and oxidation, respectively. Fatty acid uptake was increased ~20–50% in unstimulated and LPS/IFN-γ–treated $Slc2a1^{M-/-}$ BMDMs compared with controls (Fig. 1G, $p < 0.05$ in unstimulated and $p < 0.001$ in LPS/IFN-γ treatments, $Slc2a1^{fl/fl}$ versus $Slc2a1^{M-/-}$). As we have previously observed (11), oleate oxidation was greatly reduced in LPS/IFN-γ–stimulated $Slc2a1^{fl/l}$ BMDMs compared with unstimulated and IL4-stimulated BMDM. However, oleate oxidation was increased by $Slc2a1$ deficiency in both unstimulated ($p < 0.01$) and IL4-activated BMDMs ($p < 0.0001$) (Fig. 1H, $Slc2a1^{fl/fl}$ versus $Slc2a1^{M-/-}$). In summary, MΦs lacking GLUT1 displayed severely impaired glucose use and increased reliance upon alternate substrates, such as fatty acids. Remarkably, despite the absence of GLUT1, no compensatory upregulation of glucose transporter function was detected.

Slc2a1 deficiency impaired activation-associated metabolic reprogramming of MΦs

To further investigate the metabolic impact of GLUT1 depletion, we next measured substrate metabolism and mitochondrial capacity in $Slc2a1^{fl/fl}$ versus $Slc2a1^{M-/-}$ BMDMs using the Seahorse bioanalyzer. Glycolysis stress tests demonstrated that control BMDMs behaved as expected, with the greatest glycolysis, glycolytic capacity, and glycolytic reserve in LPS/IFN-γ–stimulated cells (Fig. 2). Following glucose injection, a large increase in glycolysis was detected, which increased to the highest rates after oligomycin inhibition of ATP synthase (i.e., respiration) as we have observed previously (11). Unstimulated and IL-4–polarized floxed control BMDMs displayed lower rates of glycolysis
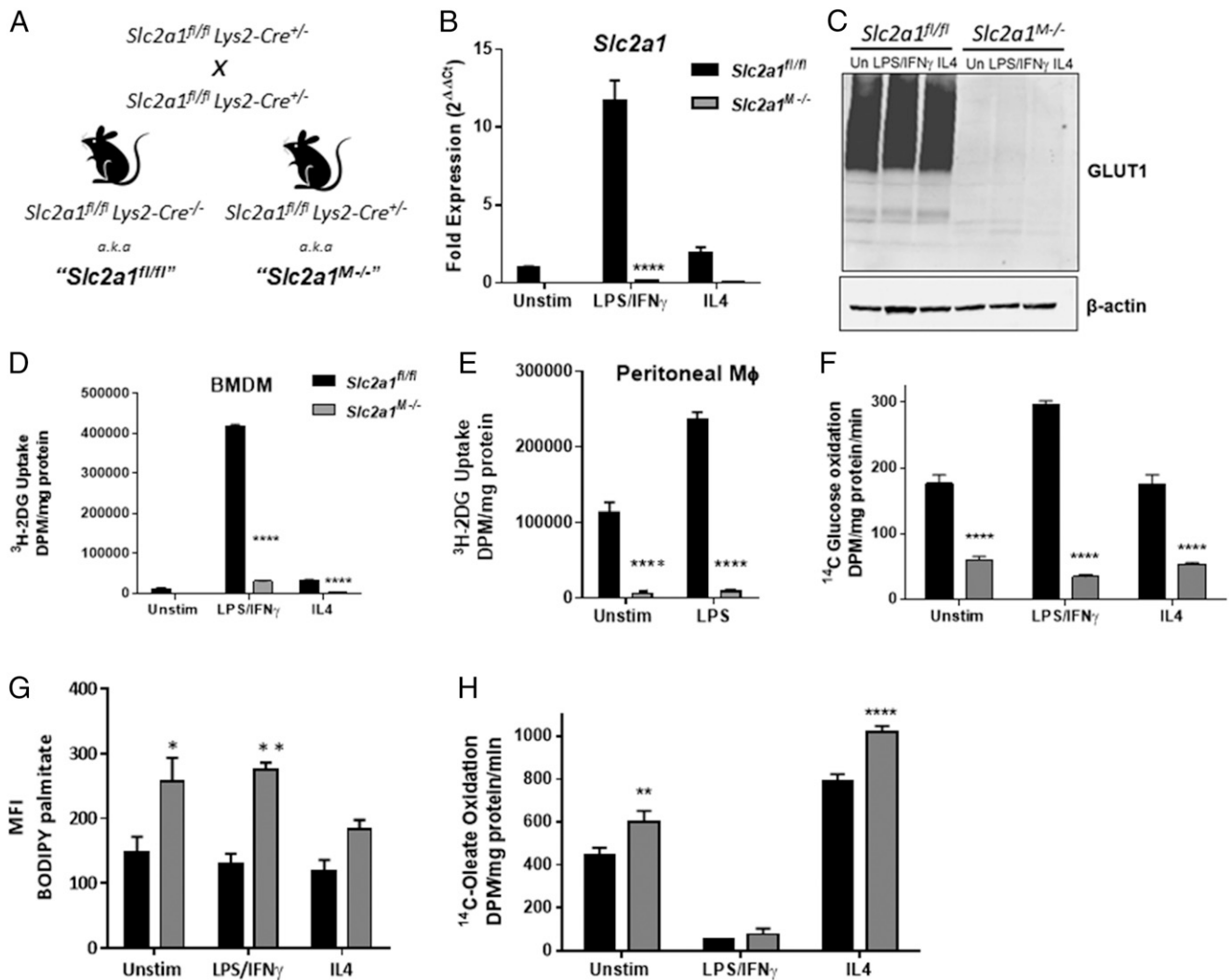
FIGURE 1. *Slc2a1* deficiency led to metabolic reprogramming of MΦs. (**A**) Generation of murine model and breeding schema. BMDMs from *Slc2a1^{fl/fl}* and *Slc2a1^{M−/−}* mice were generated. BMDMs were either left unstimulated (unstim) or treated with 5 ng/ml LPS and 10 ng/ml IFN-γ or 10 ng/ml IL-4 for 24 h. (**B**) qPCR measure of *Slc2a1* mRNA. (**C**) GLUT1 protein was measured by Western immunoblot with β-actin as loading control. GLUT1 is glycosylated, leading to large smear. (**D** and **E**) ^{3}H–2-DG uptake was measured over 10 min in BMDMs (D) and thioglycollate-elicited peritoneal MΦs (E). (**F**) ^{14}C-glucose oxidation was measured over 120 min. (**G**) BODIPY-palmitate uptake was measured by flow cytometry. (**H**) ^{14}C-oleate oxidation was measured over 120 min. Representative data out of $n = 4–5$ experiments is shown as mean ± SEM. ****$p < 0.0001$, **$p < 0.01$, *$p < 0.05$ comparing *Slc2a1^{fl/fl}* versus *Slc2a1^{M−/−}*.

compared with M1-like LPS/IFN-γ activation, as expected. The lack of GLUT1 resulted in a reduced ECAR in *Slc2a1^{M−/−}* relative to *Slc2a1^{fl/fl}* control BMDMs over the time course (Fig. 2A). In the basal state (from 0 to 20 min), the absence of GLUT1 reduced the ECAR only in LPS/IFN-γ–treated BMDMs. After glucose and oligo injections, *Slc2a1^{M−/−}* BMDMs in every activation condition (i.e., unstimulated, LPS/IFN-γ, and IL4) displayed significantly reduced ECAR. Statistical analysis for each treatment and genotype at each time point for metabolic traces are included as Supplemental Table I. In sum, BMDM lacking GLUT1 displayed significant reductions in glycolysis, glycolytic capacity, and glycolytic reserve in the LPS/IFN-γ–stimulated state (Fig. 2B, $p < 0.01$, <0.0001, and <0.0001, respectively, for *Slc2a1^{fl/fl}* versus *Slc2a1^{M−/−}*). There were no significant changes due to genotype in nonglycolytic acidification (50).

Next, mitochondrial stress tests were used to determine potential changes in oxidative metabolism driven by ablation of GLUT1 (Fig. 2C). *Slc2a1^{fl/fl}* BMDMs behaved as expected: LPS/IFN-γ–stimulated floxed control BMDMs exhibited a low OCR relative to unstimulated or IL4-stimulated cells and less responsiveness to injections to manipulate oxidative metabolism.

In contrast, IL4-stimulated floxed control BMDMs exhibited the highest maximal respiration upon FCCP-induced uncoupling compared with unstimulated and LPS/IFN-γ–stimulated floxed control BMDMs (Fig. 2C, 2D). Lack of GLUT1 did not significantly alter OCR in LPS/IFN-stimulated *Slc2a1^{M−/−}* BMDMs versus floxed controls. The absence of GLUT1 in *Slc2a1^{M−/−}* BMDMs significantly reduced maximal respiratory capacity in both unstimulated and IL4-stimulated cells compared with control *Slc2a1^{fl/fl}* BMDMs (Fig. 2C, $p < 0.01$ and <0.0001 at time points indicated for *Slc2a1^{fl/fl}* versus *Slc2a1^{M−/−}*). Overall basal and maximal respiration, proton leak, ATP production, and coupling efficiency percentage were not significantly altered by *Slc2a1* genotype (data not shown). However, significant reductions in spare respiratory capacity percentage were detected in BMDMs lacking GLUT1 compared with controls in the unstimulated and IL4-stimulated, but not LPS/IFN-γ–stimulated (highly glycolytic) states (Fig. 2D, $p < 0.01$ or $p < 0.001$, *Slc2a1^{fl/fl}* versus *Slc2a1^{M−/−}*). Finally, lack of GLUT1 also led to a significant reduction in nonmitochondrial respiration (51) in unstimulated and LPS/IFN-γ–stimulated BMDMs (Fig. 2D, $p < 0.05$ and $p < 0.01$, respectively, *Slc2a1^{fl/fl}* versus *Slc2a1^{M−/−}*).
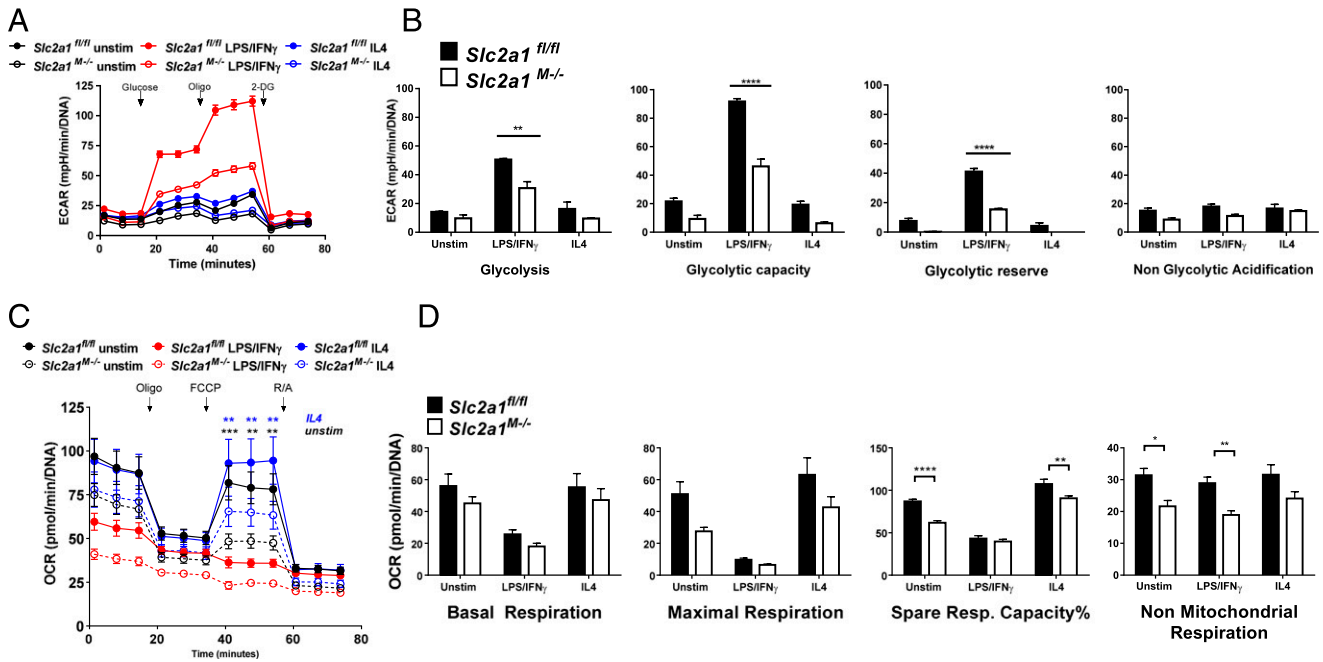
FIGURE 2. The absence of GLUT1 blunted glycolysis and reduced maximal respiration in BMDMs. Glycolysis (**A** and **B**) and mitochondrial (**C** and **D**) stress tests were used to measure the contribution of GLUT1 to BMDM metabolism. Unstimulated (unstim), LPS/IFN-γ–, or IL-4–stimulated BMDMs were analyzed on a Seahorse XF96 Extracellular Flux Analyzer, and data were normalized to DNA content. Measures were compared by two-way ANOVA for each time across genotypes and treatments [see Supplemental Table I for p values for treatment and genotype at each time in (A) and (C)]. For (B) and (D), only genotype statistical differences are depicted in graphs for clarity as *$p < 0.05$, **$p < 0.01$, ***$p < 0.001$, ****<0.0001 $Slc2a1^{fl/fl}$ versus $Slc2a1^{M-/-}$. Means + SEM are shown, with $n = 12$–24 replicates from $n = 3$ experiments.

Finally, [U-^{13}C]-glutamine metabolic tracer analysis was conducted to determine the contribution of glutamine to intermediary metabolism as an alternate substrate when glycolysis is blunted in cells lacking GLUT1 compared with controls. Labeling of cell lysates by [U-^{13}C]-glutamine was identical between $Slc2a1^{fl/fl}$ controls and $Slc2a1^{M-/-}$ BMDMs, demonstrating that the precursor pool of glutamine was equally labeled between genotypes. M+5 isotope in glutamate and α ketoglutarate (αKG) and M+4 in aspartate, succinate, fumarate, malate, citrate/isocitrate, and *cis*-aconitate were the most abundant isotopes relative to the total MID, demonstrating forward tricarboxylic acid cycle metabolism (Fig. 3A, 3B). Isotopes not shown in Fig. 3 were either nondetectable in the labeled pool or very minor and were not regulated by genotype but are depicted in Fig. 3B. GLUT1-deficient BMDMs displayed significantly increased contribution of glutamine to tricarboxylic acid cycle intermediates, starting with glutamate M+5, which demonstrated an 18% greater enrichment in GLUT1-deficient versus control BMDMs ($p < 0.05$). An 8% increase was also detected in αKG M+5, whereas its by-product, aspartate M+4, was 32% greater ($p < 0.0001$) in GLUT1-deficient BMDMs compared with controls. Similarly, both fumarate M+4 (11% greater, $p < 0.05$) and malate M+4 (15% greater, $p < 0.01$) were elevated in the absence of GLUT1. Twenty-four percent significantly greater enrichment of citrate/isocitrate M+4 was measured in GLUT1-deficient BMDM ($p = 0.0001$ control versus $Slc2a1^{M-/-}$). The intermediate between citrate and isocitrate, *cis*-aconitate M+4, was also 24% greater ($p < 0.0001$) in GLUT1-deficient cells versus controls in line with glutamine-derived forward tricarboxylic acid cycle metabolism. In contrast, succinate M+4 demonstrated a 23% significantly reduced fractional enrichment in $Slc2a1^{M-/-}$ BMDMs compared with controls ($p < 0.0001$), suggesting dilution of label by anaplerotic substrates. Finally, citrate/isocitrate M+2 (40% greater, $p = 0.0001$) and aspartate

M+2 (55% greater, $p < 0.05$) was measured in $Slc2a1^{M-/-}$, demonstrating some contribution of acetyl-CoA–derived carbons from fatty acid or other substrates, such as amino acids.

Lack of GLUT1 reduced intracellular metabolites within glycolysis and the PPP

To further elucidate the underlying effects of GLUT1 on MΦ substrate metabolism, comprehensive metabolomic profiling was undertaken. $Slc2a1^{fl/fl}$ and $Slc2a1^{M-/-}$ BMDMs were isolated and left unstimulated or activated with LPS/IFN-γ and then lysed for metabolite analysis. Principal component analysis revealed that unstimulated and LPS/IFN-γ–stimulated BMDMs were metabolically distinct with regard to genotype (Fig. 4A). Therefore, we first compared LPS/IFN-γ–stimulated $Slc2a1^{fl/fl}$ control BMDMs to unstimulated $Slc2a1^{fl/fl}$ control cells. Of 329 biochemicals measured, LPS/IFN-γ activation in $Slc2a1^{fl/fl}$ control BMDMs significantly increased 90 metabolites relative to unstimulated controls, whereas 99 were downregulated ($p < 0.05$, Supplemental Table II includes all metabolites quantities, two-way ANOVA results, and respective p values). Consistent with existing literature (9, 26, 52, 53), several metabolic intermediates were increased by LPS/IFN-γ treatment compared with unstimulated $Slc2a1^{fl/fl}$ cells in central carbon metabolism pathways, including metabolites of glycolysis, PPP, and tricarboxylic acid cycle (see cartoons and graphs in Figs. 5, 6, [$p < 0.05$, $p < 0.0001$], and Supplemental Table II).

We next compared specific GLUT1-driven genotype effects on metabolism by investigating $Slc2a1$-mediated differences between unstimulated and LPS/IFN-γ–stimulated BMDMs metabolites. In unstimulated BMDMs, lack of GLUT1 upregulated 23 and downregulated 110 metabolites compared with floxed controls ($p < 0.05$, Supplemental Table II). In LPS/IFN-γ–stimulated BMDMs, there were 82 upregulated and 78 downregulated metabolites in $Slc2a1^{M-/-}$ compared with $Slc2a1^{fl/fl}$ BMDMs
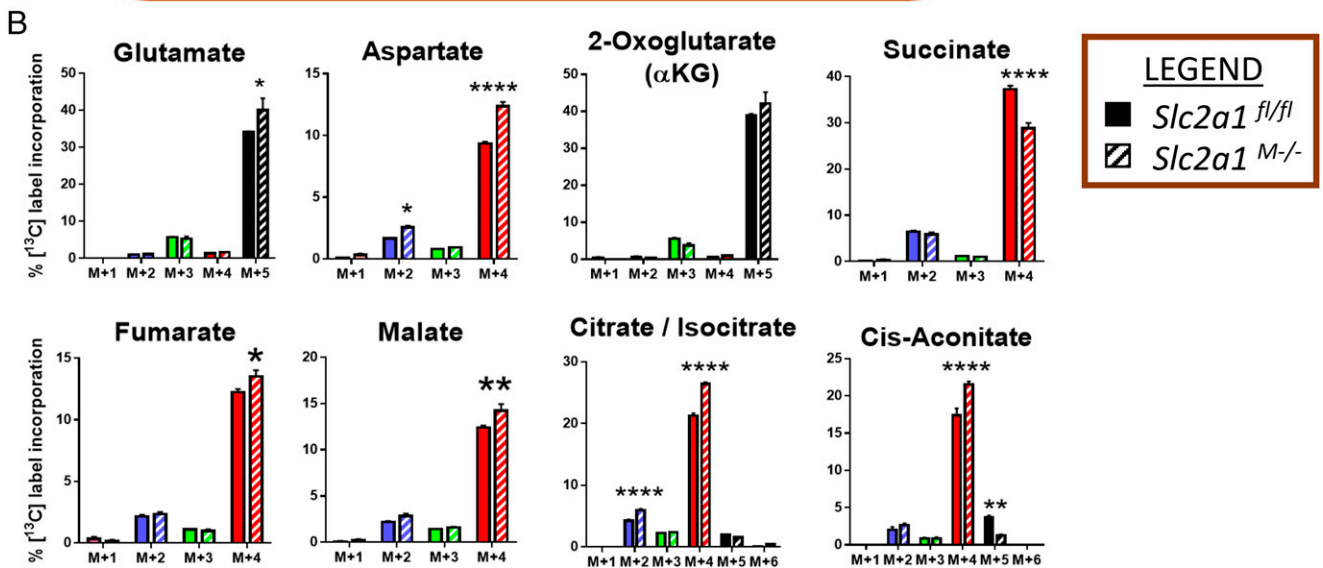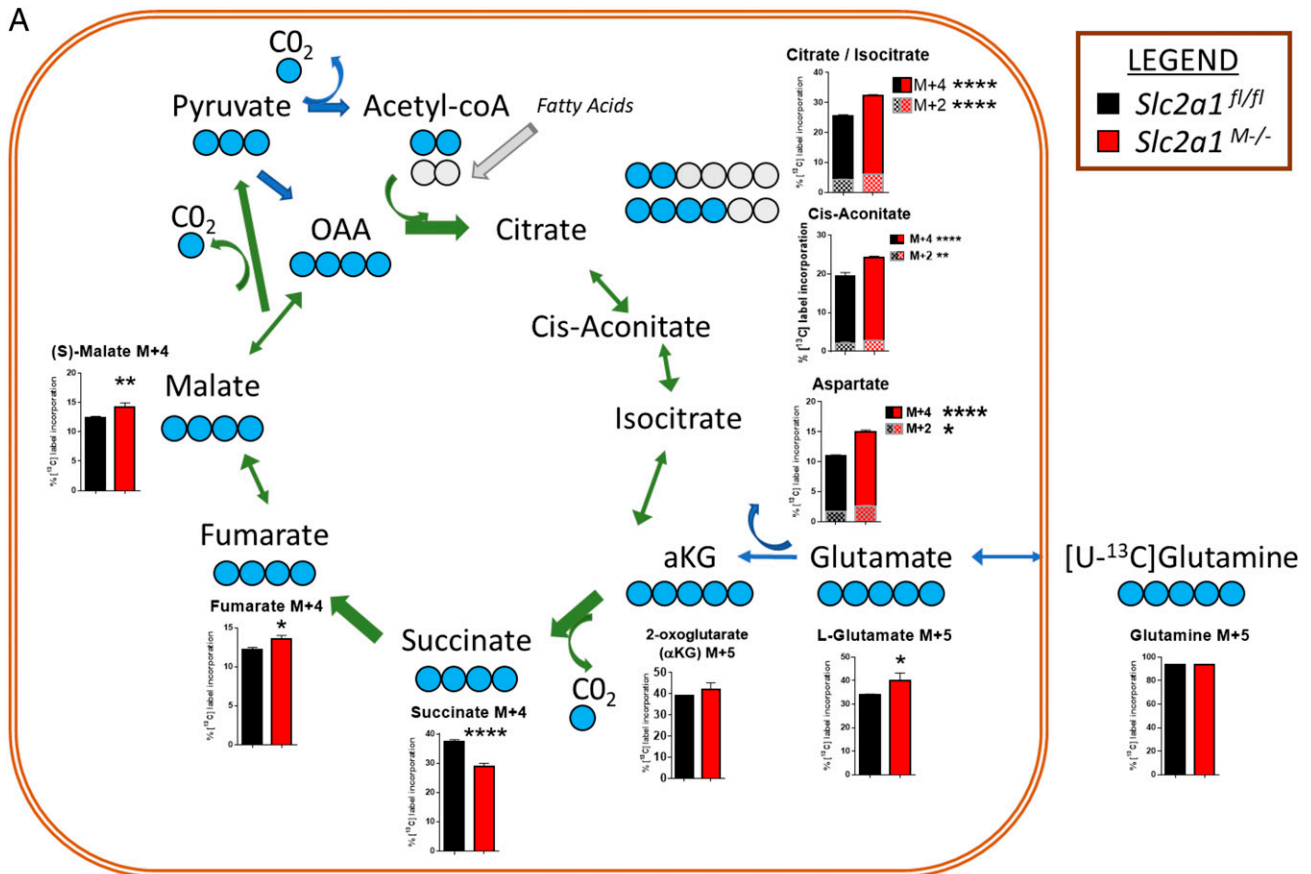
FIGURE 3. GLUT1 deletion in MΦs increased the contribution of glutamine to tricarboxylic acid cycle intermediates. (**A**) BMDMs from age-matched littermate $Slc2a1^{fl/fl}$ and $Slc2a1^{M-/-}$ mice were stimulated with LPS/IFN-γ and labeled with [U-^{13}C]-glutamine (five blue dots represent labeled carbons). Fractional enrichments of predominant isotopes M+2 or M4 are shown for each metabolite. Isotopic labeling is noted above for each of the bar graphs. Gray dots represent carbons coming from other substrates. For clarity, isotopic enrichments minimally contributing to the total pool are not shown in the tricarboxylic acid cartoon, but all are depicted in (**B**). $n = 3$ per genotype in one tracer study. The p values by two-way ANOVA are indicated above the bars in graphs or next to the legend. ****$p < 0.0001$, **$p < 0.01$, *$p < 0.05$ for $Slc2a1^{fl/fl}$ versus $Slc2a1^{M-/-}$.

($p < 0.05$). Critically, both unstimulated and LPS/IFN-γ–stimulated $Slc2a1^{-/-}$ BMDMs exhibited reduced glucose metabolism, particularly through the PPP, compared with $Slc2a1^{fl/fl}$ control BMDM, supporting findings from metabolic phenotyping above. Interestingly, in unstimulated BMDMs, glucose was significantly decreased in $Slc2a1^{M-/-}$ compared with $Slc2a1^{fl/fl}$ BMDMs (Figs. 5, 6, [$p < 0.05$, $p < 0.0001$], Supplemental Table II). In both unstimulated and

LPS/IFN-γ–stimulated BMDMs, lack of GLUT1 led to significant reductions in glucose 6-P and fructose 6-P (Fig. 5, $p < 0.05$, $p < 0.0001$). Other glycolytic metabolites, such as fructose 1,6PP and lactate, were reduced in both states but only reached significance in either unstimulated ($p < 0.001$) or LPS/IFN-γ–stimulated ($p < 0.0001$) BMDMs, respectively (Fig. 5, $p < 0.05$, $p < 0.0001$). In contrast, in unstimulated MΦs, concentrations of

FIGURE 4. *Slc2a1* deficiency altered metabolic profile and expression of inflammatory and metabolically relevant genes in MΦs. BMDMs from *Slc2a1*$^{fl/fl}$ and *Slc2a1*$^{M−/−}$ age-matched littermates were generated. (**A**) Principle component analysis was conducted after metabolomics on *Slc2a1*$^{fl/fl}$ and *Slc2a1*$^{M−/−}$ BMDMs treated as unstimulated (Unstim) or LPS/IFN-γ stimulated. $n = 4$ per genotype. All metabolites and *p* values are in Supplemental Table II. (**B**) Heatmap representing gene expression in BMDMs treated with 5 ng/ml LPS and 10 ng/ml IFN-γ for 24 h. $n = 4$ per genotype. Yellow is upregulated, and blue is downregulated. Pathways, genes, and *p* values are in Supplemental Table III for unstimulated, LPS/IFN-γ–, and IL-4–stimulated BMDMs.
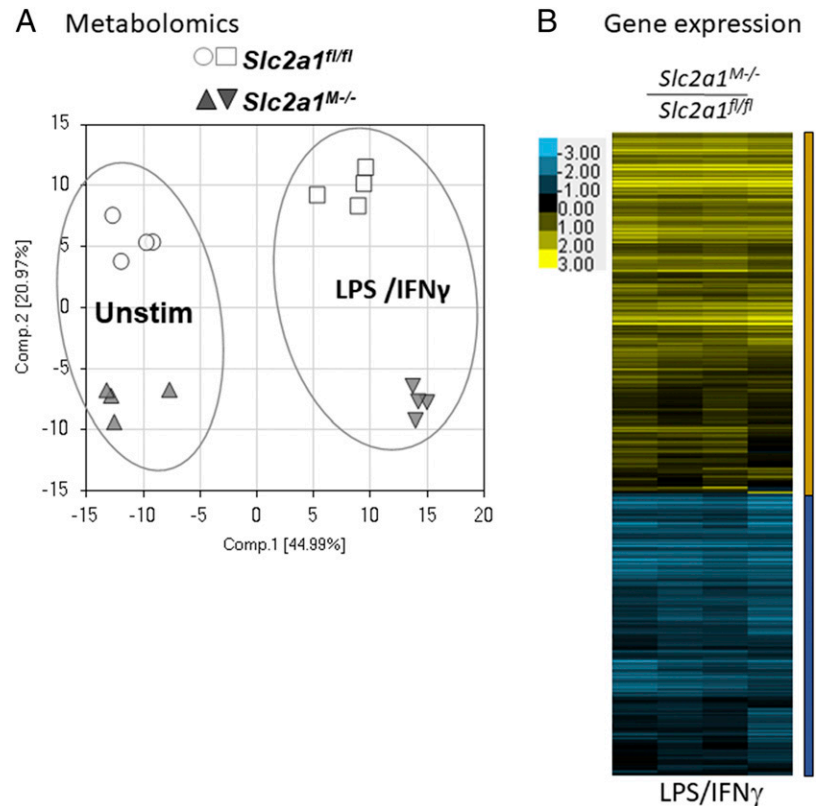
the three-carbon glycolytic intermediates 3-phosphoglycerate, 2-phosphoglycerate, and phosphoenolpyruvate were significantly greater in the absence of GLUT1 compared with *Slc2a1*$^{fl/fl}$ control BMDMs (Fig. 5, $p < 0.05$, $p < 0.0001$). Furthermore, in response to LPS/IFN-γ stimulation, the PPP intermediates 6-phosphogluconate, ribulose-5-P/xylulose 5P, ribose-5 P, ribose, ribitol, and sedoheptulose-7-P, as well as the peripheral metabolites xylitol and UDP-glucuronate, were significantly decreased by lack of GLUT1 in *Slc2a1*$^{M−/−}$ compared with *Slc2a1*$^{fl/fl}$ BMDMs (Fig. 6, $p < 0.05$, $p < 0.0001$). These data demonstrated that lack of GLUT1 reduced glycolytic and PPP intermediates.

Analysis of tricarboxylic acid cycle intermediates demonstrated increases in the absence of GLUT1: citrate, isocitrate, succinate, and fumarate were increased in GLUT1-deficient cells with LPS/IFN-γ stimulation (Supplemental Table II and *p* values within; $p < 0.05$ to $p < 0.0001$). Succinate precursor γ-aminobutyrate was also increased in *Slc2a1*$^{M−/−}$ compared with *Slc2a1*$^{fl/fl}$ BMDMs ($p < 0.05$ in the unstimulated state). Anaplerotic substrates such as glutamate and glutamine were reduced in unstimulated *Slc2a1*$^{M−/−}$ compared with *Slc2a1*$^{fl/fl}$ BMDMs ($p < 0.0001$). In addition, most amino acids were dramatically reduced in both unstimulated and stimulated states in the absence of GLUT1 (Supplemental Table II and *p* values within; $p < 0.05$ to $p < 0.0001$). Taken together, metabolomics data demonstrated a dramatic shift in BMDMs lacking GLUT1 away from glycolysis and PPP, with compensatory increased oxidation of other substrates, such as fatty acids and amino acids such as glutamine (Supplemental Table II).

GLUT1 ablation shifted arginine metabolism and polyamine synthesis in response to activating stimuli

A typical biomarker of classical versus alternative MΦ activation is arginine metabolism. Citrulline is produced from arginine as a coproduct with NO by inducible NO synthase (iNOS) (*Nos2*) upon proinflammatory activation (11, 20). Thus, we next investigated the effect of GLUT1 ablation on arginine metabolism and polyamine synthesis. Citrulline was significantly decreased by 50% in LPS/IFN-γ–stimulated BMDMs lacking GLUT1 (Supplemental Fig. 1, $p < 0.0001$). In contrast, ornithine and 4-hydroxyproline were significantly increased in LPS/IFN-γ–stimulated *Slc2a1*$^{M−/−}$ compared with *Slc2a1*$^{fl/fl}$ BMDMs (Supplemental Fig. 1, $p < 0.0001$). Additionally, the polyamines putrescine, spermidine, and spermine were dramatically increased with LPS/IFN-γ stimulation in the absence of GLUT1 compared with control BMDMs (Supplemental Fig. 1, Supplemental Table II, $p < 0.0001$). In the stimulated state, if arginine metabolism is considered as a ratio of its metabolites, citrulline to ornithine, an estimate of classical activation (high citrulline to low ornithine) versus alternative activation (low citrulline to high ornithine) can be obtained. The ratio of citrulline to ornithine was a mean of 3.52 in floxed controls and only 1.02 in BMDMs lacking GLUT1, driven by low citrulline and high ornithine in *Slc2a1*$^{M−/−}$ BMDMs compared with floxed controls (Supplemental Table II). Collectively, the described changes in arginine metabolites further support a role for GLUT1-mediated glucose metabolism in metabolic reprogramming of MΦs following exposure to proinflammatory activating stimuli.

Lack of GLUT1 reduced expression of genes associated with inflammatory signaling and markers of oxidative stress

Substrate metabolism regulates MΦ phenotype (6, 11, 12, 19, 54, 55), and in the absence of GLUT1, MΦs displayed a substrate switch from glucose to fatty acid and glutamine metabolism. Thus, we next used unbiased expression analysis to identify genes with altered expression. BMDMs were either left unstimulated or treated with 5 ng/ml LPS and 10 ng/ml IFN-γ or 10 ng/ml IL-4 for 24 h, as above, and isolated mRNA was analyzed by microarray analysis. The majority of genes were regulated by classical activation of BMDM (Supplemental Table III). Of note, unstimulated MΦs did not exhibit many GLUT1-dependent changes aside from four genes that were downregulated in *Slc2a1*$^{M−/−}$ compared with *Slc2a1*$^{fl/f}$ BMDMs,
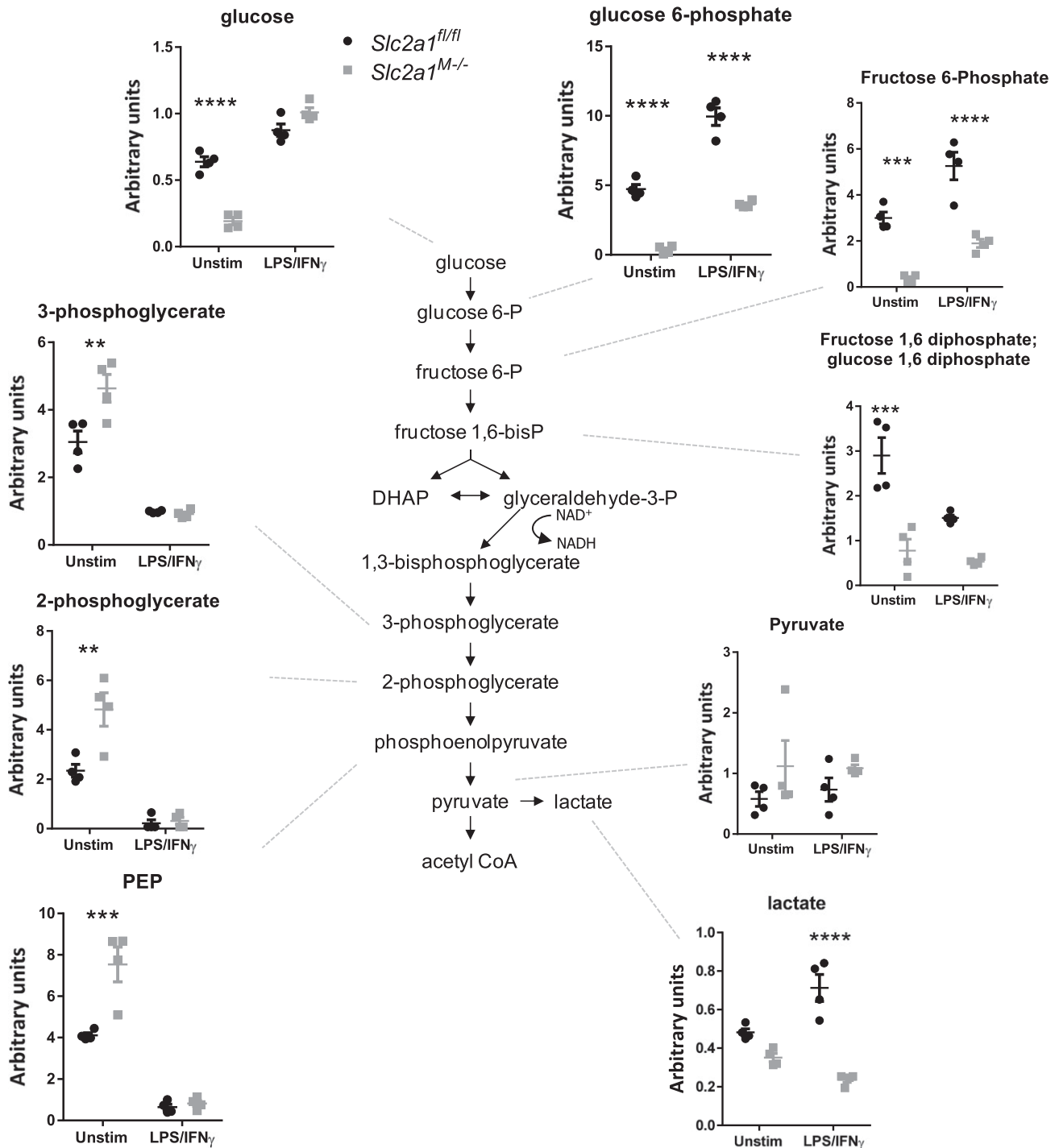
FIGURE 5. Metabolomic analysis revealed GLUT1-dependent glycolysis. BMDMs from $Slc2a1^{fl/fl}$ and $Slc2a1^{M-/-}$ age-matched littermates were generated. BMDMs were left unstimulated (Unstim) or stimulated with 5 ng/ml LPS and 10 ng/ml IFN-γ for 24 h. Metabolomic analysis was conducted, and each metabolite is labeled. $n = 4$ per genotype. Some metabolites are repeated in Figs. 5 and 6 for clarity. All metabolites and p values are in Supplemental Table II. Some p values for diet effects were omitted for clarity in figures. ****$p < 0.0001$, ***$p < 0.001$, **$p < 0.01$, $Slc2a1^{fl/fl}$ versus $Slc2a1^{M-/-}$.

namely lysozyme 2 (*Lyz2*; with two probe sets NM_017372 and ENSMUST00000092163), activating transcription factor 7 (*Atf7*), and lysozyme 1 (*Lyz1*). Likewise, only a handful of genes were regulated by GLUT1 in IL4-activated MΦs, including *Lyz2* (ENSMUST00000092163), *Lyz2* (NM_017372), *Lyz1*, *Atf7*, as well as arginase 1 (*Arg1*), which were downregulated in $Slc2a1^{M-/-}$ compared with $Slc2a1^{fl/fl}$ BMDMs.

In LPS/IFN-γ–stimulated MΦs, a heat map representing 1376 and 1080 genes up- and downregulated, respectively, showed that two major groups of genes were differentially regulated by

GLUT1 (Fig. 4B). Importantly, no glucose transporters of the SLC family were differentially regulated by GLUT1 (Supplemental Table III). Ingenuity Pathway Analysis revealed that the pathways most strongly upregulated in LPS/IFN-γ–stimulated BMDMs in the absence of GLUT1 included EIF2 signaling, regulation of eIF4 and p70S6K signaling, mTOR signaling, unfolded protein response, protein ubiquitination pathway, phagosome maturation, Ag presentation pathway, oxidative phosphorylation, and mitochondrial dysfunction (all pathways are reported in Supplemental Table III, $p < 0.05$). Notably, anti-inflammatory defenses were increased in
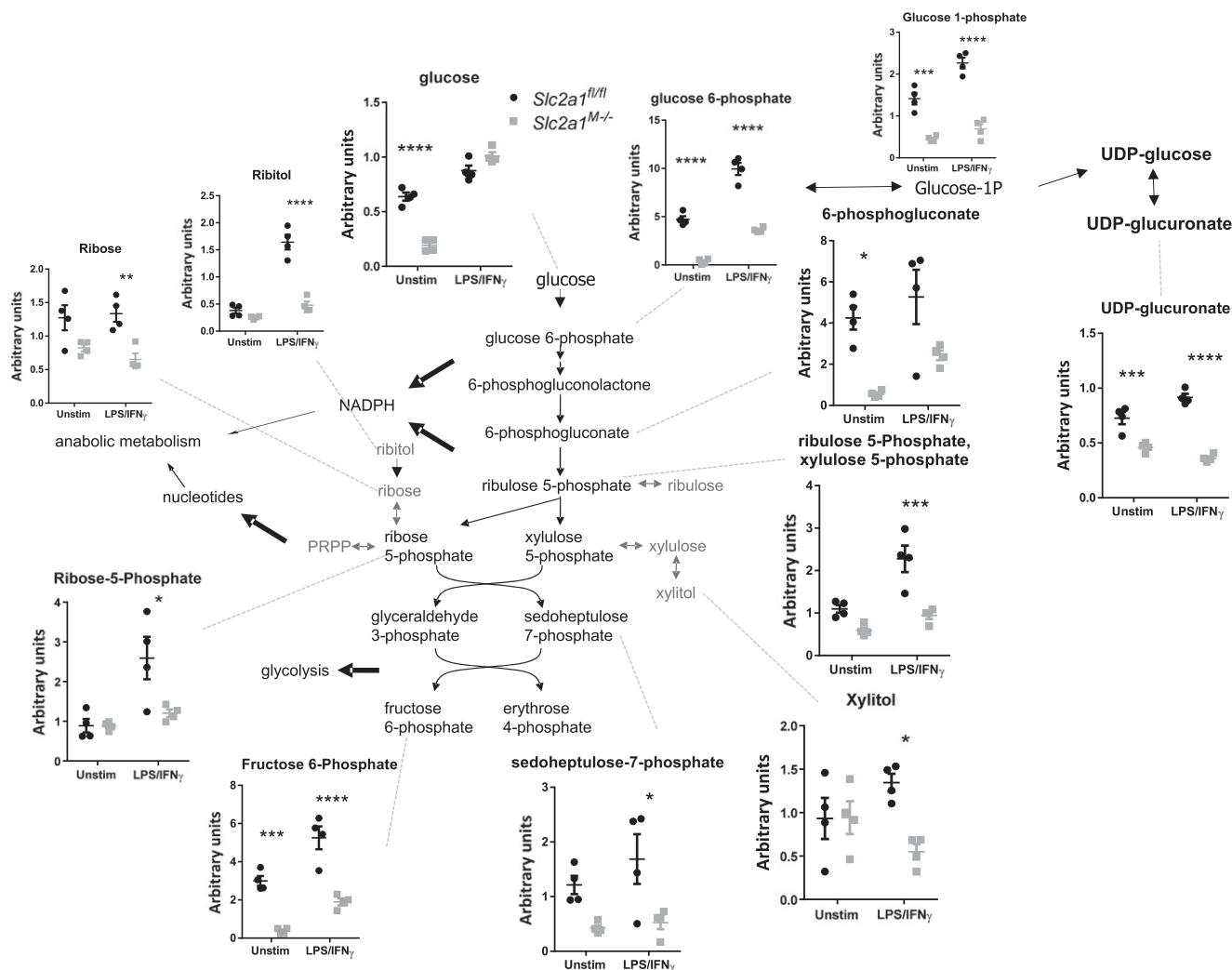
FIGURE 6. GLUT1-directed PPP in MΦs. BMDMs from *Slc2a1*$^{fl/fl}$ and *Slc2a1*$^{M-/-}$ age-matched littermates were generated. BMDMs were left unstimulated (Unstim) or stimulated with 5 ng/ml LPS and 10 ng/ml IFN-γ for 24 h. Metabolomic analysis was conducted, and each metabolite is labeled. $n = 4$ per genotype. Some metabolites are repeated in Figs. 4 and 6 for clarity. All metabolites and *p* values are in Supplemental Table II. Some *p* values for diet effects were omitted for clarity in figures. ****$p < 0.0001$, ***$p < 0.001$, **$p < 0.01$, *$p < 0.05$ *Slc2a1*$^{fl/fl}$ versus *Slc2a1*$^{M-/-}$.

the absence of GLUT1, including inhibitor of NF-κB (*Nfkbib*), which blunts LPS-activated TLR signaling (TLR4) (56). Kratz et al. (4) reported that p62/SQSTM1 was upregulated in metabolically activated MΦs to promote lipid metabolism and limit inflammation. We also observed upregulation of *Sqstm1* in *Slc2a1*$^{M-/-}$ compared with *Slc2a1*$^{fl/f}$ BMDMs, supporting metabolic and cytokine findings.

Ingenuity Pathway Analysis also revealed downregulation of pathways related to ROS and intracellular signaling in LPS/IFN-γ–stimulated *Slc2a1*$^{M-/-}$ compared with *Slc2a1*$^{fl/f}$ BMDMs, including phospholipase C signaling, production of NO and ROS in MΦs, protein kinase A signaling, and integrin signaling (all pathways are reported in Supplemental Table III, $p < 0.05$). Downregulated genes included genes related to glycolysis and the PPP, such as hexokinase (*Hk1*) and hexose-6-phosphate dehydrogenase (glucose 1-dehydrogenase, *H6pd*). A particularly striking decrease was observed in *Stat1*, a transcriptional activator and important mediator in the proinflammatory IFN-γ receptor signaling cascade. Finally, integration of gene expression and metabolite identifiers (including fold values) were used to generate pathways that were most regulated by GLUT1 (Table I, $p < 0.05$). Regulation of both genes and metabolites supported pathway analysis, including GLUT1-mediated regulation glutathione (GSH) (oxidative stress pathway), glycolysis,

arginine, and proline metabolism. Taken together, expression analysis showed that deletion of *Slc2a1* resulted in a less-inflammatory, potentially immunosuppressive phenotype, with upregulation of lipid-metabolizing and anti-inflammatory genes such as Nfkbib or p62/SQSTM1 as well as downregulation of proinflammatory glycolytic and STAT1/IFN-γ–driven pathways.

We next investigated the role of GLUT1 in immune activation. First, flow cytometric quantification of ROS in live BMDMs demonstrated significantly reduced ROS in *Slc2a1*$^{M-/-}$ compared with *Slc2a1*$^{fl/fl}$ BMDMs under both unstimulated and LPS/IFN-γ–stimulated conditions (Supplemental Fig. 2A, 2B, $p < 0.05$). Second, we compared GSH and oxidized GSSG concentrations from metabolomic analysis, as a higher GSH/GSSG ratio indicates less oxidative stress and a greater capacity to manage oxidative insult. In GLUT1-deficient BMDMs, a significantly increased GSH/GSSG ratio was observed in LPS/IFN-γ stimulation compared with *Slc2a1*$^{fl/fl}$ controls, indicative of reduced oxidative stress (Supplemental Fig. 2C, $p < 0.01$). Additionally, metabolomic analysis of methionine sulfoxide, a stable biomarker of oxidative stress (57), indicated significantly decreased concentrations in unstimulated *Slc2a1*$^{M-/-}$ BMDMs (Supplemental Fig. 2D, $p < 0.05$ comparing *Slc2a1*$^{M-/-}$ to *Slc2a1*$^{fl/fl}$). Third, assessment of inflammatory cytokines and enzymes by qPCR revealed reduced

Table I. Integrating metabolites and gene expression reveals which pathways are most significantly ($p < 0.05$) regulated by GLUT1

Pathway	Total	Expected	Hits	*p* Value
Aminoacyl-tRNA biosynthesis	91	12.0	30	0.00000059
GSH metabolism	79	10.4	27	0.00000099
Glycolysis/gluconeogenesis	89	11.7	26	0.0000400
Galactose metabolism	55	7.2	18	0.00013
Amino sugar and nucleotide sugar metabolism	85	11.2	24	0.00014
Arginine and proline metabolism	102	13.4	27	0.00019
Alanine, aspartate, and glutamate metabolism	58	7.6	18	0.00028
Purine metabolism	237	31.2	48	0.00093
PPP	49	6.5	14	0.0032
Butirosin and neomycin biosynthesis	7	0.9	4	0.0075
Citrate cycle (tricarboxylic acid cycle)	51	6.7	13	0.012
Pyruvate metabolism	65	8.6	15	0.019
Glycosaminoglycan degradation	22	2.9	7	0.019
Valine, leucine, and isoleucine biosynthesis	13	1.7	5	0.020
Pyrimidine metabolism	139	18.3	27	0.021
Sphingolipid metabolism	68	9.0	15	0.028
Biosynthesis of unsaturated fatty acids	29	3.8	8	0.029
Nicotinate and nicotinamide metabolism	41	5.4	10	0.036
Fructose and mannose metabolism	59	7.8	13	0.039
Starch and sucrose metabolism	66	8.7	14	0.045

Kyoto Encyclopedia of Genes and Genomes metabolite and GenBank gene numbers and fold changes ($Slc2a1^{-/-}/Slc2a1^{fl/fl}$) were entered into Metaboanalyst for pathway analysis.

LPS/IFN-γ–stimulated PAI1 (*Serpine1*, $p < 0.05$) expression in $Slc2a1^{M-/-}$ BMDMs (Fig. 7A). Notably, PAI-1 is known to be regulated by GLUT1 (11). Expression of iNOS (*Nos2*), a common biomarker of classical M1-like activation, was reduced by over 50% in LPS/IFN-γ–stimulated $Slc2a1^{M-/-}$ BMDMs compared with $Slc2a1^{fl/fl}$ BMDMs (Fig. 7B, $p < 0.0001$). Moreover, in cells lacking GLUT1, proinflammatory chemokine MCP-1 (*Ccl2*) was also significantly reduced at both the mRNA (data not shown) and protein concentration (Fig. 7D, $p < 0.05$). In contrast, *Arg1*, a marker of M2-like alternative activation upon IL4 stimulation, was also reduced in the absence of GLUT1, suggesting that both M1- and M2-like biomarkers were reduced (Fig. 7C, $p < 0.0001$). Interestingly, IL-1β displayed an increase in the absence of GLUT1 in LPS/IFN-γ–stimulated cells (Fig. 7D, $p < 0.0001$). There were no significant changes in other

cytokines, including IL6, IL10, or TNF-α (Fig. 7D). Taken together, these data suggest an overall reduction in activation in both M1- and M2-like enzymes with reduced MCP1 chemokine but no major reductions in typical inflammatory cytokines in the absence of GLUT1.

Obese $Slc2a1^{M-/-}$ mice display elevated markers of visceral adipose MΦ infiltration without associated metabolic sequelae

Obesity is a chronic inflammatory disease in which elevated MΦ content in visceral adipose tissue is an established driver of metabolic dysfunction. Hence, we next investigated if a lack of myeloid *Slc2a1* would reduce HFD-induced obesity and/or impair the development of obesity-associated sequelae. Male $Slc2a1^{M-/-}$ and $Slc2a1^{fl/fl}$ mice were randomly weaned onto a LFD (10% calories from fat) or HFD (45% calories from fat). Body weights
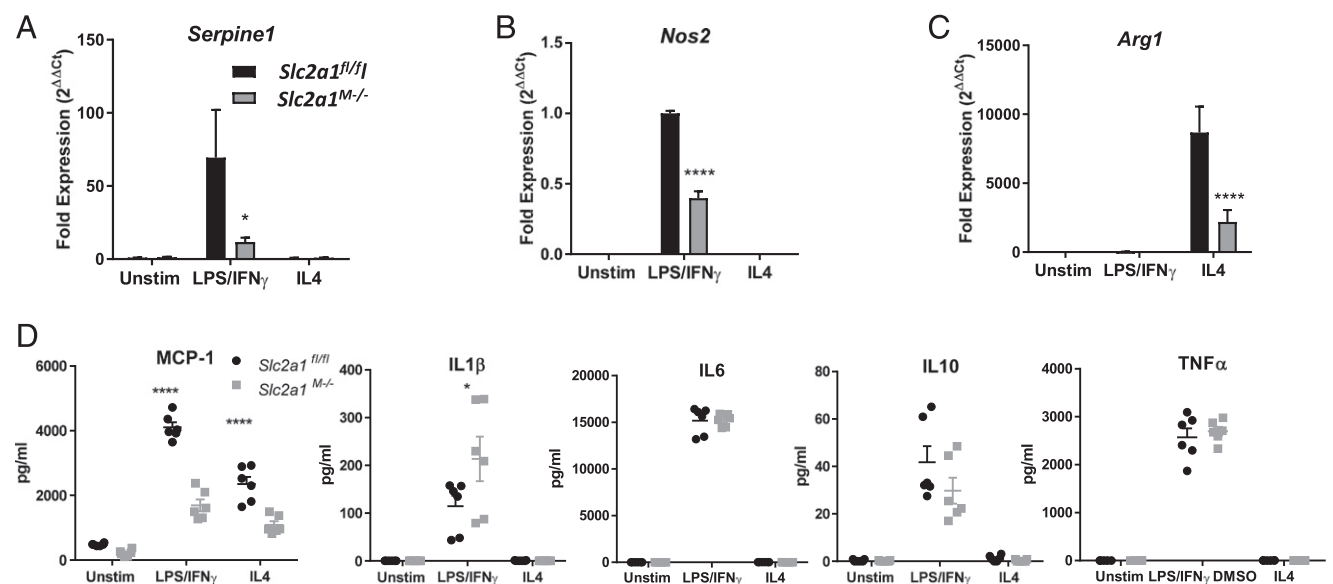
FIGURE 7. Lack of GLUT1 led to reduced activation. BMDMs from $Slc2a1^{fl/fl}$ and $Slc2a1^{M-/-}$ age-matched littermates were generated. BMDMs were left unstimulated (Unstim) or stimulated with 5 ng/ml LPS and 10 ng/ml IFN-γ or 10 ng/ml IL-4 for 24 h. (**A–C**) qPCR analysis was conducted on M1-like markers, including *Serpine1* (PAI-1), *Nos2* (iNOS), and M2-like marker *Arg1*. $n = 3$ replicates in three experiments. (**D**) Luminex protein analysis was used to measure concentrations from conditioned media of chemokine *Ccl2* (MCP-1), and cytokines IL1β, IL6, Il10, and TNF-α. Mean ± SEM is shown. $n = 4–6$. ****$p < 0.0001$, *$p < 0.05$ $Slc2a1^{fl/fl}$ versus $Slc2a1^{M-/-}$.

were significantly greater in HFD-fed mice compared with LFD-fed mice, as expected, starting at 3 wk following diet start in $Slc2a1^{fl/fl}$ mice and 7 wk in $Slc2a1^{M-/-}$ mice (Fig. 8A, *$p < 0.01$, LFD versus HFD). Interestingly, from 5 wk on diet until sacrifice, lean $Slc2a1^{M-/-}$ mice were significantly heavier than lean $Slc2a1^{fl/fl}$ controls (Fig. 8A, $p < 0.05$). Notably, $Slc2a1^{fl/fl}$ mice developed fasting hyperglycemia on a HFD (Fig. 8B, $p < 0.01$), whereas $Slc2a1^{M-/-}$ mice did not. However, although glucose tolerance and insulin tolerance were impaired following prolonged HFD exposure, no genotype-driven effects were observed (data not shown). Body composition as measured by MRI demonstrated HFD-induced fat accretion with elevated, but nonsignificant, increases in fat mass in $Slc2a1^{M-/-}$ compared with $Slc2a1^{fl/fl}$ mice (Fig. 8C). HFD exposure increased eWAT pad mass equally in $Slc2a1^{fl/fl}$ and $Slc2a1^{M-/-}$ mice (Fig. 8D, $p < 0.001$ in $Slc2a1^{fl/fl}$ mice and $p < 0.0001$ in $Slc2a1^{M-/-}$ mice, comparing LFD versus HFD). There were no significant effects of GLUT1 deficiency on lean mass for either diet (data not shown). Similarly, measurement of liver and brown adipose tissue weights indicated significantly increased mass of both in HFD-fed mice ($p < 0.0001$), yet no significant GLUT1-mediated effects were observed (data not shown). Additionally, energy expenditure experiments using metabolic cages

did not reveal significant differences driven by GLUT1 in lean or obese mice (data not shown).

Interestingly, despite a lack of significant genotype-driven differences in weight gain, body composition, or fat pad mass in obese $Slc2a1^{M-/-}$ mice compared with floxed controls, eWAT in $Slc2a1^{M-/-}$ mice displayed 5-fold elevated MCP-1 (Ccl2) expression compared with $Slc2a1^{fl/fl}$ mice (Fig. 8E, $p < 0.001$). Adipose MΦ infiltration was next analyzed via expression of MΦ marker Emr1 (F4/80) and immunohistochemical analysis of F4/80+ MΦ staining. Emr1 mRNA expression was more than doubled in HFD-fed $Slc2a1^{M-/-}$ mice compared with $Slc2a1^{fl/fl}$ mice (Fig. 8F, $p < 0.001$). Immunohistologic detection of F4/80 indicated that although there was no genotype effect within diet, CLS were increased by a HFD in obese compared with lean $Slc2a1^{M-/-}$ mice, whereas no significant diet effect was observed for $Slc2a1^{fl/fl}$ mice (Fig. 8G, 8H, $p < 0.0001$ LFD versus HFD in $Slc2a1^{M-/-}$ mice).

Therefore, to investigate the long-term effects of GLUT1 ablation on adipose MΦ infiltration, a subset of mice was maintained on a LFD or HFD for ~10 mo (an average of 46.13 wk; $n = 4$ per diet and genotype). At this time point, older, obese, HFD-fed $Slc2a1^{fl/fl}$ and $Slc2a1^{M-/-}$ mice both exhibited significantly increased body weight and fasting glucose relative to lean animals, with no
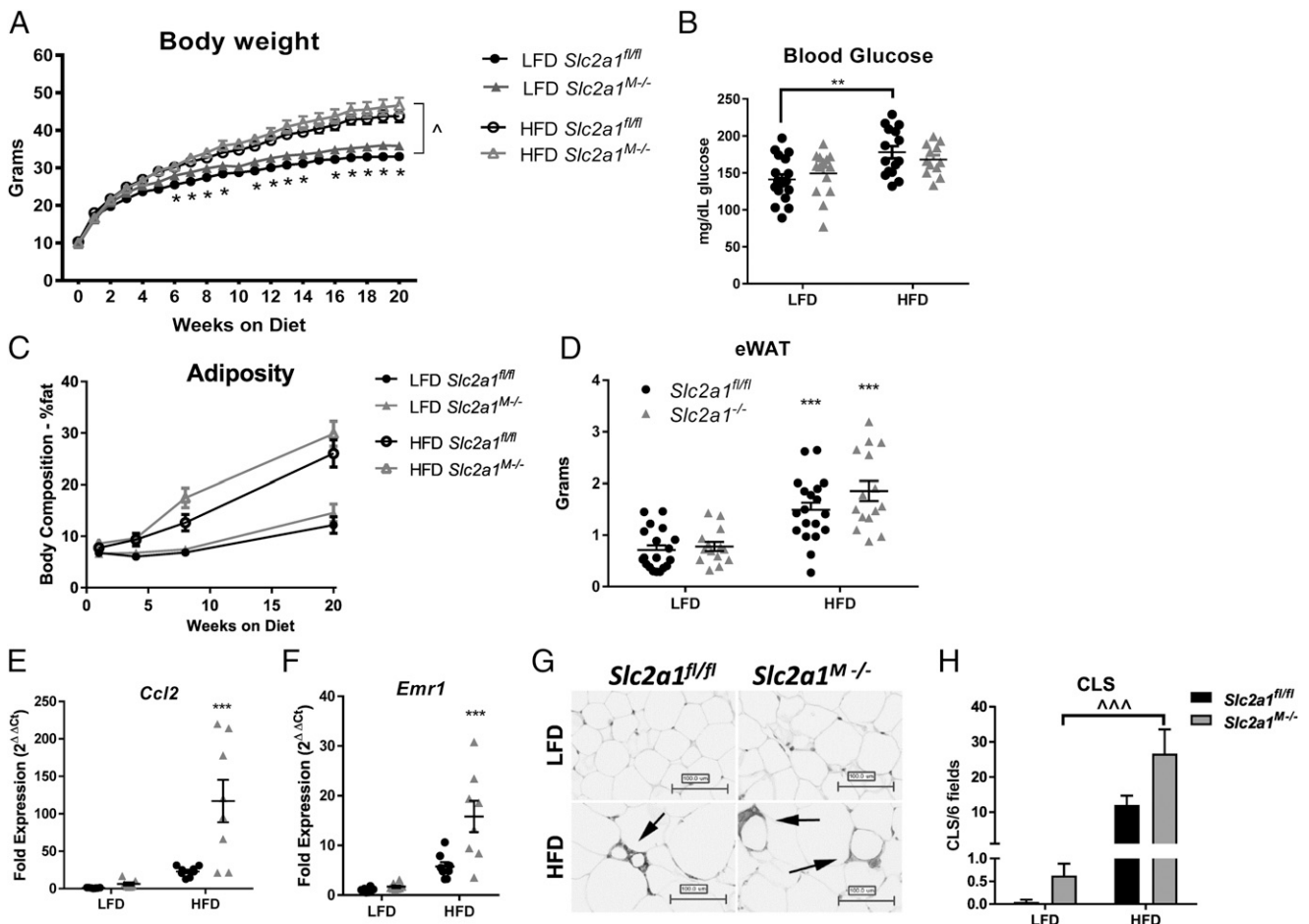

FIGURE 8. Obese $Slc2a1^{M-/-}$ mice displayed greater chemokine expression and greater markers of MΦ infiltration in eWAT. Age-matched $Slc2a1^{fl/fl}$ and $Slc2a1^{M-/-}$ littermates were weaned onto 10% (LFD) and 45% (HFD) kcal from fat diets at 3 wk of age and maintained on diet. (**A**) Body weight was measured as indicated. ^$p < 0.05$ in $Slc2a1^{fl/fl}$ LFD mice versus HFD mice from 3 wk until harvest and in $Slc2a1^{M-/-}$ LFD mice versus HFD mice from 7 wk until harvest. *$p < 0.05$ $Slc2a1^{fl/fl}$ versus $Slc2a1^{M-/-}$ in LFD only. (**B**) Six hours fasted blood glucose at 21 wk of age. $p < 0.01$ LFD versus HFD. ***$p < 0.001$ and ****$p < 0.0001$ HFD versus LFD. (**C**) MRI analysis of adiposity was quantified at 1, 4, 7, and 20 wk on diet. (**D**) eWAT was weighed at sacrifice. ***$p < 0.001$, $Slc2a1^{fl/fl}$ versus $Slc2a1^{M-/-}$. (**E** and **F**) qPCR analysis of eWAT expression of chemokine Ccl2 (MCP1) and MΦ marker Emr1 (F4/80). ***$p < 0.001$, $Slc2a1^{fl/fl}$ versus $Slc2a1^{M-/-}$. (**G**) F4/80+ immunohistochemical analysis of eWAT. CLS are indicated by arrows. Representative images shown (original magnification ×20). Scale bar, 100 μm. (**H**) CLS were quantified in six random F4/80+ stained fields. ^^^$p < 0.0001$ for LFD versus HFD in $Slc2a1^{M-/-}$ mice compared with $Slc2a1^{fl/fl}$ mice. $n = 14$–19 mice.

significant differences by genotype (data not shown). Interestingly, despite an ~2-fold difference in total adiposity, eWAT mass did not significantly differ between lean and obese animals following prolonged obesity (Supplemental Fig. 3A, 3B). However, adipose pads of older obese mice exhibited discoloration that was not observed in lean animals (image in Supplemental Fig. 3B) or younger obese mice from previous analyses. Individual eWAT pads were collected and dissociated for flow cytometric analysis of total adipose immune invasion, total myeloid cell content, and MΦ content. Total stromal-vascular cells in obese mice were elevated ~3-fold relative to lean mice, with no genotype-driven difference detected (Fig. 9A). Similarly, total CD45$^+$ immune cell content as a percentage of stromal-vascular cells was not significantly altered by diet or genotype (Fig. 9B), nor was CD11b$^+$ myeloid cell content as a percentage of total immune cells (Fig. 9C). However, as a percentage of myeloid cell content, CD64$^+$ MΦs were increased nearly 2-fold in obese mice (Fig. 9D), which translated to a dramatic increase in the number of MΦs per gram of adipose (Fig. 9E). Neither adipose MΦ content nor percent contribution to the myeloid fraction was altered by

the absence of GLUT1. Together, these results indicate that GLUT1 ablation did not alter adipose infiltration by MΦs or other myeloid subsets potentially affected by LysMCre-driven $Slc2a1$ deletion. However, lack of GLUT1 increased expression of CD64 (FcγRI) in adipose MΦs of both lean and obese $Slc2a1^{M-/-}$ mice relative to $Slc2a1^{fl/fl}$ controls (Fig. 9F, ****$p < 0.0001$, lean versus obese; $p = 0.022$ $Slc2a1^{fl/fl}$ versus $Slc2a1^{M-/-}$). CD64 is a definitive MΦ marker, and its expression has been reported to be modulated by both IFN-γ and IL-10, suggesting roles in both inflammatory response and resolution following insult. Percentage of adipose MΦs expressing CD206 was not influenced by diet or genotype (Supplemental Fig. 3C, 3D), but MΦ CD206 expression was elevated in response to GLUT1 ablation in lean animals (Fig. 9G, $p = 0.040$, $Slc2a1^{fl/fl}$ versus $Slc2a1^{M-/-}$), indicating increased CD206 surface expression by individual MΦs. Interestingly, this increase in CD206 expression was not observed in obese $Slc2a1^{M-/-}$ mice. Overall, these data show that myeloid GLUT1 deletion does not dramatically influence systemic metabolism or immune infiltration of visceral adipose in response to prolonged obesity, even in aged mice. However, findings
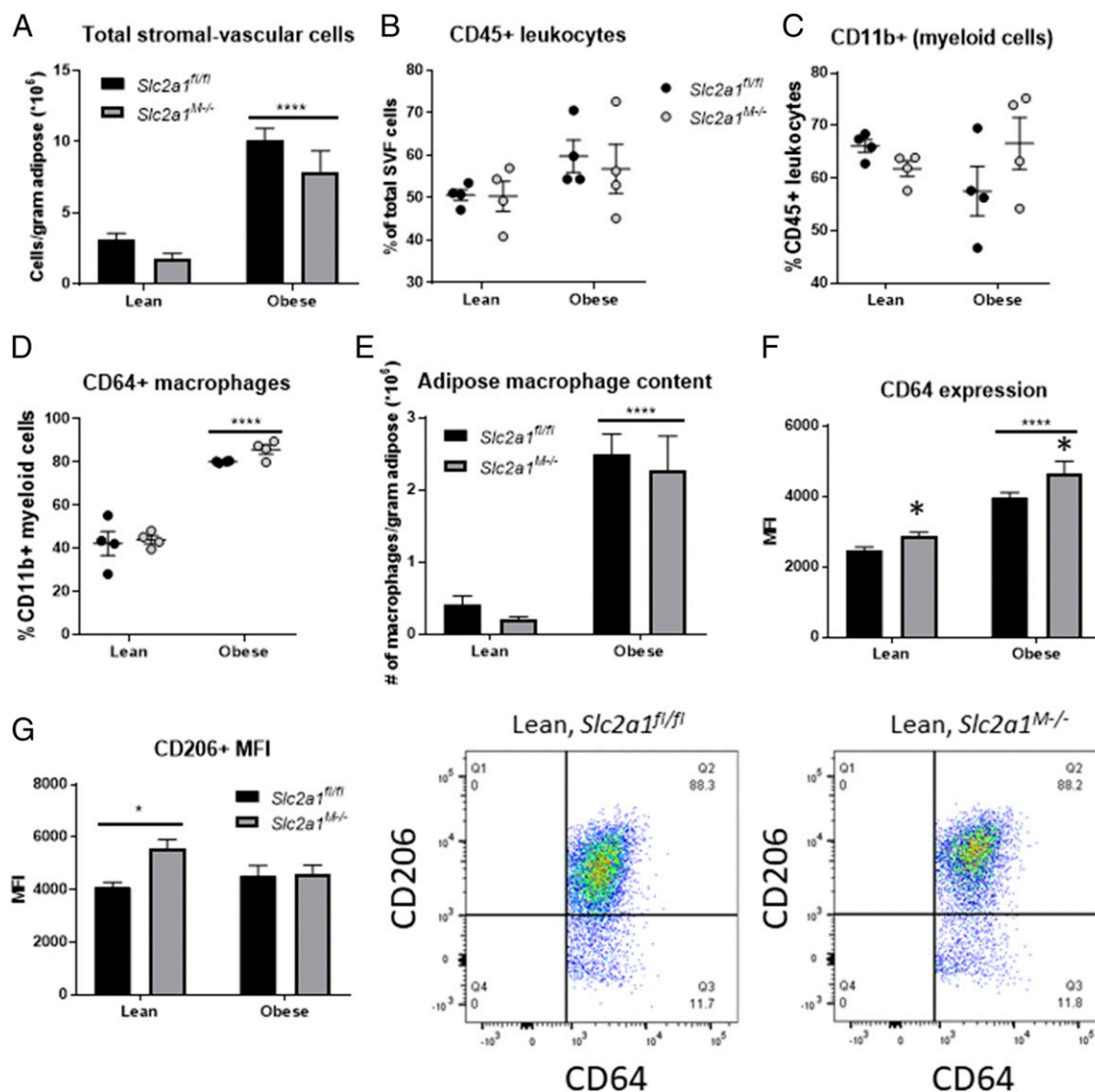
FIGURE 9. Myeloid-specific GLUT1 ablation affected phenotype, but not infiltration, of adipose tissue MΦs in older mice. (**A**) Total cell count within the SVF was normalized to eWAT mass. ****$p < 0.0001$, lean versus obese. (**B**) CD45$^+$ leukocytes as a percentage of total SVF cells. (**C**) CD11b$^+$ myeloid cells as a percentage of total (CD45$^+$) adipose leukocytes. (**D**) CD64$^+$ MΦs as a percentage of total (CD11b$^+$) myeloid cells. ****$p < 0.0001$, lean versus obese. (**E**) Adipose tissue MΦ content was calculated as the number of MΦs per gram of tissue. ****$p < 0.0001$, lean versus obese. (**F**) CD64 expression quantified as MFI. ****$p < 0.0001$, lean versus obese; *$p = 0.022$ $Slc2a1^{fl/fl}$ versus $Slc2a1^{M-/-}$. (**G**) CD206 expression quantified as MFI. *$p = 0.040$, $Slc2a1^{fl/fl}$ versus $Slc2a1^{M-/-}$. Representative pseudo-color dot plots shown for lean mice. $n = 4$ per diet and genotype.

suggest phenotypic differences in MΦs lacking GLUT1, such as elevated expression of canonical MΦ markers, suggest the potential for as-yet undetected alterations in adipose tissue homeostasis.

Myeloid GLUT1 deficiency decreased stability of atherosclerotic plaques

As expression of MΦ-associated inflammatory mediators and metabolism is also crucial in atheroma formation, we hypothesized that MΦ contribution to atherogenesis may be altered by GLUT1 deficiency. To determine the effects of a lack of *Slc2a1* on atherogenesis, bone marrow from *Slc2a1*^{fl/fl} and *Slc2a1*[M−/−] donors was transplanted into 10-wk-old lethally irradiated mice lacking LDL receptor (*Ldlr*^{−/−}). Control unreconstituted *Ldlr*^{−/−} recipient mice (transplanted with vehicle HBSS buffer only) died by 10–11 d after irradiation, confirming successful endogenous bone marrow depletion (data not shown). Four weeks after reconstitution, *Slc2a1*^{fl/fl} *Ldlr*^{−/−} and *Slc2a1*[M−/−] *Ldlr*^{−/−} mice were exposed to Western diet for the remainder of the study to induce atherogenesis (58) (see study design in Supplemental Fig. 4A). Deletion of myeloid *Slc2a1*

did not alter the susceptibility of *Ldlr*^{−/−} mice to gain weight (Supplemental Fig. 4B) or change fasting plasma glucose over the course of the study (Supplemental Fig. 4C) compared with *Slc2a1*^{fl/fl} *Ldlr*^{−/−} mice. Similarly, *Slc2a1*[M−/−] *Ldlr*^{−/−} mice did not exhibit altered systolic or diastolic blood pressure at 16 wk of age relative to *Slc2a1*^{fl/fl} *Ldlr*^{−/−} control mice (data not shown). Finally, deletion of myeloid *Slc2a1* did not alter body composition of recipient mice (i.e., percentage of lean or fat mass) as measured by MRI at 5, 10, 16, and 22 wk of age, corresponding to before BMT, before diet, 6 wk on diet, and at sacrifice after 12 wk on diet (data not shown). Interestingly, total cholesterol (Supplemental Fig. 4D, $p < 0.0196$) and LDL cholesterol (Supplemental Fig. 4E, $p < 0.017$) concentrations in plasma after 12 wk on Western diet were 20 and 23% greater, respectively, in *Slc2a1*[M−/−] *Ldlr*^{−/−} compared with control *Slc2a1*^{fl/fl} *Ldlr*^{−/−} mice. Total plasma high-density lipoprotein (HDL) and triglyceride concentrations were not altered by *Slc2a1* deletion (data not shown, respectively).

After 12 wk of diet (at 22 wk of age), mice were terminated, and aortic root lesions were analyzed. Lack of GLUT1 did not lead to
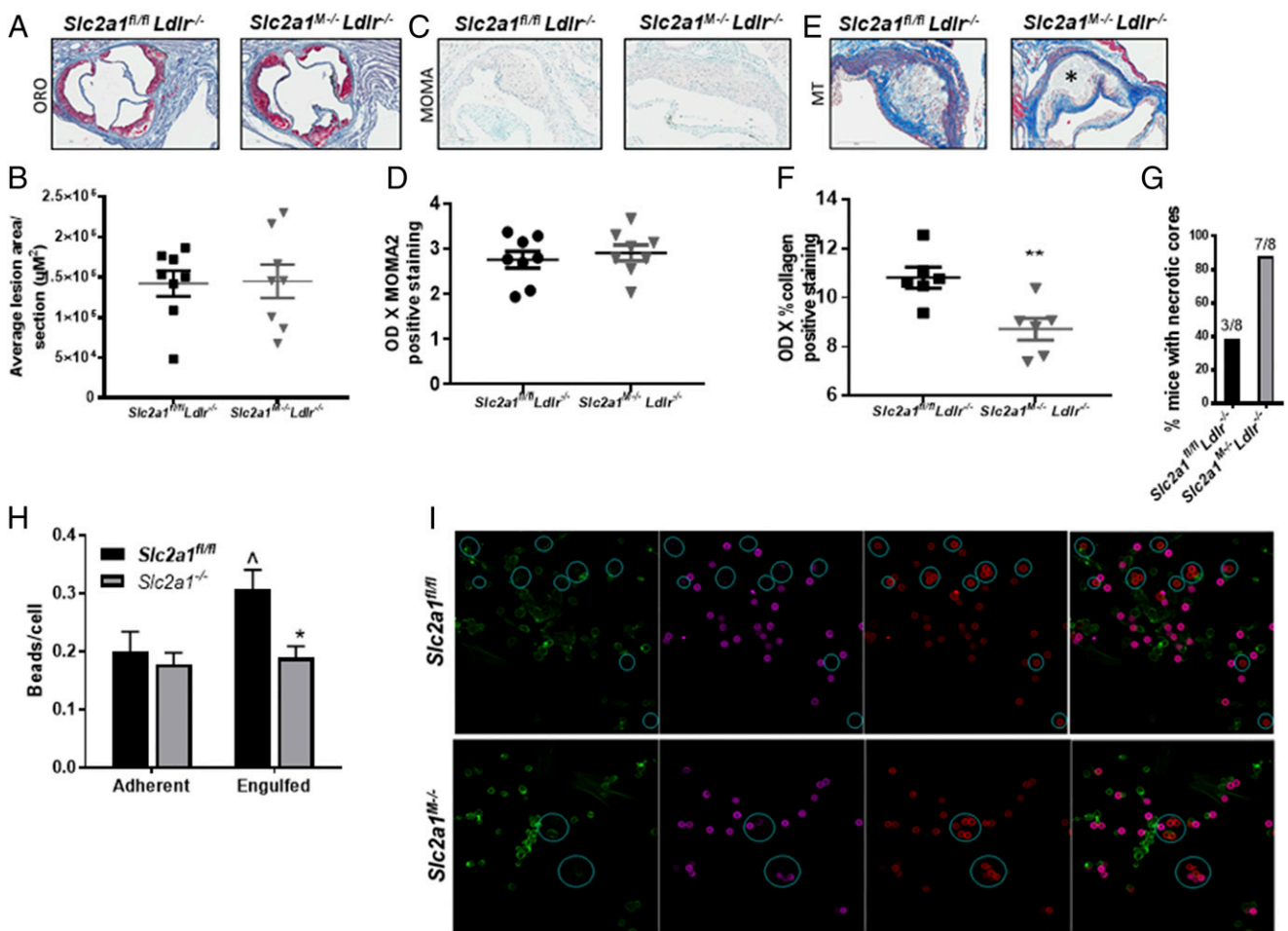

FIGURE 10. *Slc2a1*[M−/−] *Ldlr*^{−/−} mice displayed unstable lesions, and lack of GLUT1 led to phagocytic defects. Marrow from *Slc2a1*^{fl/fl} and *Slc2a1*[M−/−] mice was transplanted into *Ldlr*^{−/−}, and mice were fed a Western diet for 12 wk. (**A**) Serial interrupted 10-μm sections were stained with ORO and counterstained with hematoxylin. Representative photomicrographs (original magnification ×20) of ORO staining are shown. *n* = 8. (**B**) Quantification of lesion area. (**C**) Serial interrupted 5-μm sections were immunostained with anti-MOMA2 and counterstained with methyl green. Representative photomicrographs (original magnification ×20) are shown. *n* = 8. (**D**) Quantification of MOMA2+ content. *n* = 8. (**E**) Serial interrupted 5-μm sections were stained with Masson's trichrome (MT). Representative photomicrographs (original magnification ×20) are shown. Necrotic core indicated with asterisk (*). *n* = 8 (**F**) Quantification of collagen content. **$p < 0.01$. (**G**) Quantitative analysis of the percentage of mice with necrotic cores. (**H** and **I**) Ten-micrometer IgG-coated carboxylated microsphere adherence and uptake assay was conducted over 20 min. Fixed MΦs were stained with phalloidin-AF488 for actin (green), Rhodamine Red-X for extracellular adherent beads (magenta), and Cy5 (red) for total (adherent and engulfed) beads following permeabilization. Zeiss LSM Image Browser was used to circle engulfed 10-μm beads. Blue DAPI was not shown for clarity. (I) Quantification of adherent and engulfed beads. *$p < 0.05$, *Slc2a1*^{fl/fl}/*Ldlr*^{−/−} versus *Slc2a1*[M−/−] *Ldlr*^{−/−}. Mean ± SEM. *n* = 3–4 experiments. ^$p < 0.05$, *Slc2a1*[Fl/Fl] adherent versus engulfed beads. Representative images (original magnification ×40) are shown.

significant differences in total lesion size in the aortic root compared with control $Slc2a1^{fl/fl} Ldlr^{-/-}$ mice (Fig. 10A, 10B). There was also no GLUT1-driven difference in the number of subendothelial cells per total lesion area between $Slc2a1^{M-/-} Ldlr^{-/-}$ compared with $Slc2a1^{fl/fl} Ldlr^{-/-}$ mice (data not shown). Thus, we next quantified MOMA2-positive MΦ content. No significant differences were observed in MΦ content in lesions of $Slc2a1^{M-/-} Ldlr^{-/-}$ compared with $Slc2a1^{fl/fl} Ldlr^{-/-}$ mice (Fig. 10C, 10D). Thus far, data suggested that myeloid GLUT1 does not alter lesion size or MΦ content. However, the noncellular composition of the intimal lesions such as collagen content can alter plaque stability (59), which was, in fact, dramatically altered by $Slc2a1$ deficiency. Atheromas in $Slc2a1^{M-/-} Ldlr^{-/-}$ mice contained significantly less collagen compared with $Slc2a1^{fl/fl} Ldlr^{-/-}$ mice (Fig. 10E, 10F, $p < 0.0065$). Moreover, 87% of $Slc2a1^{M-/-} Ldlr^{-/-}$ mice displayed necrotic core formation (seven out of eight mice), compared with only 37.5% of control $Slc2a1^{fl/fl} Ldlr^{-/-}$ mice (three out of eight mice, Fig. 10G). Thus, although few systemic defects were present, significant local changes to the vessel microenvironment led to unstable necrotic lesions in the absence of myeloid GLUT1.

Finally, glucose plays an important role in actin polymerization (60) as well as MΦ clearance of apoptotic cells, a type of phagocytosis called efferocytosis (61). Altering phagocytosis of LDL/ox-LDL and/or efferocytosis could potentially influence the accumulation of necrotic material. Thus, we examined whether $Slc2a1^{M-/-}$ MΦs displayed defects in phagocytic capacity compared with $Slc2a1^{fl/fl}$ MΦs. Carboxylated microsphere phagocytosis assays were used to model particle uptake akin to efferocytosis, thereby testing the role of GLUT1 in binding and engulfment (62–64) in $Slc2a1^{fl/fl}$ and $Slc2a1^{M-/-}$ MΦs (Fig. 10H, 10I). However, whereas $Slc2a1^{fl/fl}$ MΦs engulfed beads efficiently ($p < 0.05$ adherent versus engulfed), MΦs lacking GLUT1 displayed a significantly reduced (38%) capacity to engulf microspheres (Fig. 10H, 10I, $p < 0.007$ comparing $Slc2a1^{M-/-}$ to $Slc2a1^{fl/fl}$). In summary, these results suggest that efferocytosis may be impaired in the absence of GLUT1, potentially contributing to the accumulation of necrotic debris in lesions of $Slc2a1^{M-/-}$ mice.

Discussion

A spectrum of MΦ activation phenotypes exist in tissue microenvironments that can be characterized by differential surface marker expression, cytokine repertoire, and metabolic profile (1, 8). Immune cell function is reliant upon intracellular metabolism to generate immune responses and maintain tissue homeostasis (8, 9, 65–67). We and others have shown that metabolic reprogramming and resulting substrate preference in response to activating stimuli play pivotal roles in immune cell biology, acting as a determinant of inflammatory potential in MΦs and dictating functionality of NK, T, and B cells (9, 11–13, 19, 54, 66, 68–72). Based on the importance of metabolism in determining immunophenotype and response, nutrient transporters may be excellent targets to regulate MΦ activation and subtypes, allowing these immune cells to be successfully targeted through approaches such as nanoparticle delivery (73–76).

In the current studies, we hypothesized that the glucose transporter GLUT1 acts as a gatekeeper to a robust glycolysis/PPP-associated proinflammatory response in MΦs. To this end, we successfully created a unique murine model in which glucose metabolism was blunted in a myeloid-specific manner. Indeed, in the absence of GLUT1, BMDMs and thioglycollate-elicited peritoneal $Slc2a1^{M-/-}$ MΦs failed to uptake glucose in the basal or alternatively activated states, in which glucose use is minimal. Upon LPS/IFN-γ stimulation, minimal glucose uptake was evident in BMDMs lacking GLUT1, suggesting minor uptake

was possible, likely through contaminating cells in BMDM preparation. Indeed, no increase in glucose uptake was present in thioglycollate-elicited LPS-stimulated MΦs. We have previously published that GLUT3 is expressed at the limit of detection in BMDMs and is, in fact, downregulated with LPS/IFN-γ stimulation (11). Gene expression analysis presented in this article supports that no glucose transporters of the SLC family were differentially regulated in the absence of GLUT1. Taken together, the overall lack of glucose uptake in $Slc2a1^{M-/-}$ MΦs supports that 1) GLUT1 is the primary glucose transporter in MΦs, and 2) there was no compensatory upregulation of other glucose transporters.

The metabolic impact of GLUT1 deletion on MΦ substrate use demonstrated that in the absence of GLUT1, $Slc2a1^{M-/-}$ BMDMs resorted to elevated fatty acid uptake and oxidation as well as greater glutamine oxidation. Cellular bioenergetics analysis demonstrated that glycolysis, as measured by ECAR, was dramatically blunted in the absence of GLUT1, even in response to stimuli that typically increase glycolysis (LPS/IFN-γ). OCR measurements suggested no defects in basal respiration; however, respiration was blunted by the lack of GLUT1 in the uncoupled state after FCCP injection, indicating that maximal flux through the electron transport chain was not sustainable. Interestingly, $[^{14}C]$-oleate fatty acid oxidation was elevated with specific stimuli in cells lacking GLUT1. $[U-^{13}C]$-glutamine metabolic tracer analysis determined that glutamine contributed to intermediary metabolism as an anaplerotic substrate in GLUT1-deficient BMDMs. Compared with control BMDMs, in $Slc2a1^{M-/-}$ BMDMs, most metabolites of the tricarboxylic acid cycle demonstrated significantly enriched M+4 or M+5 isotopes. Nominal but significantly enriched M+2 citrate/isocitrate and aspartate suggest glutamine contributed two carbons to the pool of citrate/isocitrate, yielding the M+2 isotope (through pyruvate and acetyl-CoA) with other carbons likely derived from substrates such as fatty acids or amino acids through acetyl-CoA in the absence of GLUT1-mediated glycolysis. Overall, tracer studies are consistent with glutamine use as an anaplerotic substrate when GLUT1 is absent. Of note, succinate enrichment was significantly reduced in $Slc2a1^{M-/-}$ BMDMs compared with controls, which could be explained by unlabeled anaplerotic substrates such as branched-chain amino acids entering at succinate through succinyl-CoA (77). Thus, further study of glutamine and branched-chain amino acid transport and metabolism with respect to GLUT1 deletion or inhibition should be evaluated. Together, these data suggest a flexibility in MΦ metabolism yet an inability to fully compensate for a lack of GLUT1. It is possible that there is a defect in mitochondrial content in the absence of GLUT1. In sum, in cells driven toward an increased dependence on glycolysis in response to LPS/IFN-γ, the lack of GLUT1 prevented glycolysis and PPP metabolism. In cells that are unstimulated or activated to be primarily oxidative with IL4 stimulation, the lack of GLUT1 hindered the ability to increase broad oxidative metabolism when needed, as demonstrated by reduced maximal respiration. Future studies will determine GLUT1-mediated changes to mitochondrial content, mitophagy, and additional analysis of specific metabolite transport and metabolism.

Comprehensive metabolomic analysis revealed that glycolytic intermediates glucose-6-P and fructose-6-P were decreased in $Slc2a1^{M-/-}$ versus $Slc2a1^{fl/fl}$ BMDMs, consistent with decreased glucose availability and reduced glycolytic flux. Additionally, we observed a dramatic decrease in nearly every PPP intermediate in $Slc2a1^{M-/-}$ BMDMs, consistent with reduced glucose availability. Of note, glucose was still detected in GLUT1-deficient BMDMs stimulated by LPS/IFN-γ, suggesting that this glucose could be accounted for by the small amount of glucose taken up by contaminating cells in the LPS/IFN-γ–stimulated BMDMs

(discussed above) or possibly created by gluconeogenesis or released by glycogenolysis, and it may be metabolized at a slower rate. Indeed, reduced expression of hexokinase 1 (*Hk1*; Supplemental Table III), ~3-fold lower concentrations of downstream metabolites in glycolysis, and reductions in ECAR together support a defect in glycolysis because the absence of GLUT1. Furthermore, complementary findings were reported in our previous work, wherein greater glucose uptake and PPP metabolites were observed in response to GLUT1 overexpression studies in MΦs (11). Reduced glycolysis in the absence of GLUT1 led us to question whether *Slc2a1*$^{M-/-}$ MΦs would show increased reliance on other metabolic pathways. In this study, significantly increased concentrations of tricarboxylic acid cycle intermediates (including citrate, isocitrate, succinate, and fumarate) were detected in *Slc2a1*$^{M-/-}$ BMDMs stimulated by LPS/IFN-γ. These elevated tricarboxylic acid cycle intermediates were likely derived from anaplerosis, such as elevated glutamine metabolism (as we demonstrated) or other substrates (9, 10, 12). An increased reliance of *Slc2a1*$^{M-/-}$ BMDMs upon anaplerotic substrates such as glutamine is further supported by the observed reductions in intracellular levels of most of the proteinogenic amino acids. Amino acid catabolism can contribute to pyruvate and other three-carbon intermediates in lower glycolysis, such as phosphoenolpyruvate, 2-PG, and 3-PG, which were elevated in cells lacking GLUT1. Dipeptides were also increased, suggesting protein degradation to fuel anaplerosis. In sum, lack of GLUT1 redirected substrate metabolism from glucose and glycolysis toward oxidative and anaplerotic metabolism.

LPS/IFN-γ–activated M1-like MΦs become metabolically reprogrammed through two main blocks, or "brakes," in the tricarboxylic acid cycle (9, 10). First, classical activation reduces expression of the enzyme isocitrate dehydrogenase (*Idh*), which leads to an accumulation of citrate (78). Citrate plays many important roles in MΦs; it can drive proinflammatory responses such as lipid synthesis necessary for Ag presentation as well as regulate ROS and/or NO production, reviewed in detail in Van den Bossche et al. (9). For instance, citrate-derived itaconate is increased by LPS/IFN-γ and is responsible for the second break in the tricarboxylic acid cycle through inhibition of succinate dehydrogenase (SDH1). Less SDH1 activity leads to reduced oxidative metabolism and allows for the increased glycolytic flux needed for proinflammatory activation (79–81) through reduced tricarboxylic acid cycle as well as SDH- containing complex II in the electron transport chain. Yet checkpoints are also in place that provide negative feedback to prevent too strong of a proinflammatory response. Itaconate itself also acts as an immunosuppressive anti-inflammatory metabolite that downregulates ROS, iNOS, and certain cytokine production (21). In this study, the observed increase in citrate in *Slc2a1*$^{M-/-}$ BMDMs compared with controls is paradoxical because citrate is typically a biomarker of classical M1-like activation, and cells lacking GLUT1 appear incapable of complete M1-like activation. In the absence of GLUT1, reduced ROS was detected even in the presence of greater concentrations of citrate relative to floxed controls. Reduced ROS in the absence of GLUT1 may be explained by the homeostatic mechanism of citrate-derived itaconate inhibiting both SDH1 and reverse electron transport–derived ROS production, as increased itaconate was also detected in cells lacking GLUT1. Taken together, our findings indicate that lack of GLUT1 prevented complete activation to a classical phenotype in response to LPS/IFN-γ stimulation and suggest a greater dependence on fatty acid metabolism, supportive of a shift toward an alternative M2-like phenotype. Future studies will entail detailed flux analysis to determine to what extent glucose versus certain fatty acids versus glutamine are metabolized in a GLUT1-regulated manner.

A main component of pro- versus anti-inflammatory MΦ phenotypes is arginine metabolism (82), which was dramatically regulated by the absence of GLUT1. In classically activated, proinflammatory MΦs, citrulline is produced from arginine as a coproduct with NO by iNOS (*Nos2*) (11, 20). NO is a highly unstable radical that nitrosylates and thereby inactivates components of the electron transport chain, which further drives glycolysis because oxidative metabolism is reduced (21). In this way, arginine acts as a central node in both inflammation and metabolism. Although NO cannot be measured directly in tissue, citrulline concentration acts as a surrogate marker for diversion of arginine toward inflammatory products. Importantly, the lack of GLUT1 in *Slc2a1*$^{M-/-}$ BMDMs reduced both cellular citrulline levels and iNOS mRNA expression compared with *Slc2a1*$^{fl/fl}$ BMDMs, supporting a role for GLUT1 in the regulation of the iNOS proinflammatory pathway. In *Slc2a1*$^{M-/-}$ GLUT1-deficient BMDMs, low citrulline levels were also concomitant with high ornithine, a shift in metabolism resembling the alternative M2-like phenotype. In alternatively activated MΦs, arginine is preferentially metabolized to ornithine, which is shunted into the synthesis of polyamines, molecules associated with extracellular matrix remodeling during wound healing or tissue growth. Importantly, polyamines are critical mediators of IL-4–induced alternative MΦ activation and greatly elevated in the absence of GLUT1 (82, 83). For example, spermine reportedly blunts LPS-induced secretion of proinflammatory cytokines in both mouse and human MΦs (84, 85), whereas polyamine-depleted MΦs show an increased inflammatory response (86–88). Additional downstream ornithine metabolites include proline and 4-hydroxyproline, both of which are also involved in matrix remodeling. The concentration of 4-hydroxyproline was greater in *Slc2a1*$^{M-/-}$ BMDM compared with concentrations in *Slc2a1*$^{fl/fl}$ BMDM. In sum, GLUT1 manipulation resulted in striking and reciprocal effects on polyamine synthesis, as evidenced by a dramatic increase in response to GLUT1 deletion (this manuscript) along with potent downregulation following GLUT1 overexpression as we previously reported (11). These findings suggest that GLUT1 deletion may hold potential for increased extracellular matrix remodeling during resolution of the inflammatory response, a hypothesis that could be tested in models of infectious disease.

In accordance with the observed GLUT1-mediated metabolic changes, GLUT1 ablation also skewed the BMDMs toward a less-activated phenotype overall. *Slc2a1*$^{M-/-}$ BMDMs failed to fully classically M1 polarize in vitro, showing reduced expression of proinflammatory mediators, including reduced iNOS and MCP1. However, GLUT1 did not alter secretion of IL6, IL10, or TNF-α. Moreover, glycolysis in classically activated MΦs has been shown to be essential for IL-1β production (9, 12), yet IL-1β was not reduced in the absence of GLUT1. In fact, it was elevated, albeit with great variability in concentrations (89, 90). Upregulation of the M2-associated enzyme *Arg1* was, in fact, blunted following IL-4 stimulation in BMDMs lacking GLUT1. Thus, similar to our metabolomics and bioenergetics findings, the GLUT1-deficient inflammatory phenotype was neither purely pronor anti-inflammatory but, instead, mixed phenotype, perhaps indicating stunted activation. A potential mechanism explaining this paradoxical phenotype was a significant reduction in STAT1 expression in MΦs deficient for GLUT1, which mediates IFN-γ signaling to polarize MΦs toward the proinflammatory phenotype (91), but these and other pathways remain to be studied in the future.

We next assessed the ability of MΦs to generate a functional immune response in the absence of GLUT1-mediated glucose availability. Metabolomic and flow cytometric analysis of ROS production showed reduced ROS and methionine sulfoxide in *Slc2a1*$^{M-/-}$ BMDMs following LPS/IFN-γ activation as well as greater capacity to combat oxidative stress (higher GSH/GSSG

ratio). Reduced oxidative stress in MΦs lacking GLUT1 is complementary to our previously published work, wherein overexpression of GLUT1 induced elevated ROS production and markers of oxidative stress (11). Interestingly, methionine sulfoxide was significantly reduced in cells lacking GLUT1 compared with $Slc2a1^{fl/fl}$ BMDMs; this metabolite is not just a marker of oxidative stress but can also lead to classical (M1) polarization in vitro (57). These findings may be explained by the reduction of flux through the PPP in cells lacking GLUT1, as PPP flux is required in classical M1-like activation for ROS (through NADPH oxidase) and NO production, yet it is not required in alternative activation (92). In sum, pathways downstream of GLUT1 that produce ROS, as well as metabolic intermediates capable of MΦ proinflammatory activation and markers of oxidative stress, were reduced in $Slc2a1^{M-/-}$ BMDMs.

Taken together, the overall phenotype of GLUT1-deficient BMDMs was primarily less proinflammatory, which led us to question the role of GLUT1 in MΦ biology in systemic disease. Obesity is associated with low-grade adipose inflammation and oxidative stress following MΦ infiltration into epididymal and brown adipose depots as well as other adipose depots including the human breast and normal mouse mammary gland (19, 20, 28, 31, 43, 93–98). Indeed, adipose tissue MΦs appear to be a unique phenotype distinct from MΦ subtypes described in other tissues (1). Early characterization of adipose tissue MΦ populations first described the obesity-induced appearance of proinflammatory MΦs in conjunction with elevated levels of proinflammatory cytokines and chemokines such as TNF-α, IL6, and CCL2 (99, 100). However, recent extensive profiling of adipose tissue MΦs from adipose tissue of obese mice and humans has revealed a "mixed" pro- and anti-inflammatory phenotype (101–106). Considering the complexity of phenotyping MΦs by surface markers and expression profiling, the contribution of underlying metabolic parameters has the potential to inform us about MΦ phenotype and function in adipose tissue of obese individuals. Therefore, we sought to determine the contribution of myeloid GLUT1 to the development of obesity and its associated inflammatory sequelae. Despite the pronounced metabolic and inflammatory changes observed in $Slc2a1^{M-/-}$ BMDMs, in vivo obesity studies unexpectedly revealed only subtle findings. $Slc2a1^{M-/-}$ mice did not display differences in body weight, body composition, or insulinemia compared with floxed controls when fed an obesogenic HFD. However, following 20 wk on a HFD, control mice developed fasting hyperglycemia compared with lean controls, whereas $Slc2a1^{M-/-}$ mice did not, suggesting protection from diet-induced defects in glycemic control, albeit subtle. In contrast, subsequent analyses did not reveal significant GLUT1-mediated differences in glucose or insulin tolerance. Interestingly, long-term exposure (>40 wk) to HFD-induced obesity resulted in hyperglycemia in both floxed control and $Slc2a1^{M-/-}$ mice, suggesting that the loss of myeloid GLUT1 prolonged development of hyperglycemia but was not fully protective against obesity-associated systemic pathological conditions, such as metabolic dysregulation. The lack of prominent genotype-driven systemic metabolic abnormalities allowed for a tissue-specific focus on the role of myeloid GLUT1 in the adipose microenvironment. Histologic and flow cytometric analyses of adipose tissue MΦs revealed no significant genotype-driven differences in adipose MΦ content in either lean or obese mice. Thus, MΦ were able to infiltrate (or proliferate) in adipose tissue even in the absence of GLUT1. Of note, a greater concentration of CCL2 was observed in the adipose tissue of $Slc2a1^{M-/-}$ mice compared with $Slc2a1^{fl/fl}$ controls. MCP-1 is known to be produced by adipocytes in obesity, suggesting that despite adequate MΦ infiltration, a distress signal continued to be secreted in the adipose tissue of myeloid GLUT1-deficient mice. Thus, GLUT1-deficient adipose tissue MΦs are present, but they are not "effective" in promoting typical comorbidities associated with obesity, such as glucose intolerance. Critically, expression of the typically M2-like alternative marker CD206 (mannose receptor) was elevated in adipose tissue MΦs from lean $Slc2a1^{M-/-}$ mice, a finding also observed at the mRNA level in in vitro, unstimulated BMDMs, which is indicative of an adipose tissue MΦ of an alternative or M2-like phenotype. Collectively, our data suggest that the phenotypic shift toward alternative M2-like adipose tissue MΦs in the absence of GLUT1 may have transiently protected mice from typical concomitant metabolic sequelae associated with obesity. However, this protection was lost with prolonged obesity in older mice. These data emphasize that despite dramatic defects in glycolysis, PPP, and ROS production, the metabolic flexibility of MΦs can compensate enough through anaplerotic and other substrate metabolism that lead to only subtle defects in diet-induced obese mice lacking myeloid GLUT1.

Because obesity and atherosclerosis share common inflammatory etiologies, we next aimed to investigate how myeloid GLUT1 affected atherosclerosis. Atherosclerosis is linked to many risk factors, including obesity (26, 107). MΦs are involved in almost every stage of atherosclerosis, with MΦ glycolysis associated with poorer outcomes (108). In the early stage, MΦs become foam cells through the unabated engulfment of lipids, clearance of neighboring dead cells (termed "efferocytosis"), and secretion of a spectrum of proinflammatory cytokines, ROS, and reactive nitrogen species. In the advanced stage, MΦs promote the death of smooth muscle cells and release matrix-degrading enzymes and procoagulant tissue factors (107, 109). Both classically and alternatively activated MΦs are present in atherosclerotic lesions (110). The proinflammatory MΦ phenotype has been reported to be associated with plaque progression, whereas the immunosuppressive M2-like phenotype is linked to reduced lesion size and plaque regression (108, 111–116). Furthermore, atheromas are also known to take up high levels of glucose (117). Therefore, using a BMT strategy, we generated mice with $LysM$Cre–driven ablation of $Slc2a1$ in an atherogenic LDL receptor–deficient model. There were no differences in lesion size in $Slc2a1^{M-/-}$ $Ldlr^{-/-}$ compared with $Slc2a^{fl/fl}$ $Ldlr^{-/-}$ mice. Minor GLUT1-dependent increases in plasma total and LDL cholesterol were also detected, findings which were paradoxical because greater plasma cholesterol concentrations typically lead to larger lesions. Of note, however, lesion composition was dramatically altered in a GLUT1-dependent manner. Lesions in mice lacking myeloid GLUT1 exhibited a greater degree of necrosis and less collagen content compared with floxed control mice, critical factors associated with lesion instability (118). Advanced lesions may or may not narrow the arterial lumen but are clinically significant because complications are more likely to develop (119). For example, pathological studies suggest that the development of thrombus-mediated acute coronary events depends principally on the composition and vulnerability of a plaque rather than the severity of stenosis (120).

MΦ glucose metabolism in atherosclerosis was previously investigated using a GLUT1 gain-of-function strategy in chimeric mice. By transplanting $Ldlr^{-/-}$ mice with MΦs overexpressing GLUT1, Nishizawa et al. (121) reported that increasing MΦ glucose metabolism by overexpressing GLUT1 did not affect any parameter of atherosclerosis, including lesion size or necrotic area. These results were interesting in light of our previous in vitro model of GLUT1 overexpression, in which GLUT1-mediated glucose metabolism was shown to play a key role in promoting MΦs to mount a robust, proinflammatory response (11).

We suspect that lesion MΦs are already highly activated—and expressing high levels of GLUT1—such that overexpression did not alter the phenotype in Nishizawa et al.'s studies. Additionally, Sarrazy et al. (117) published a partial loss of function model wherein transplant of *Slc2a1* heterozygous apolipoprotein E ($ApoE^{-/-}SLc2a1^{+/-} \rightarrow ApoE^{-/-}$) bone marrow into *ApoE*-null mice reduced lesion size and glucose uptake into lesions compared with wild-type–transplanted mice. Myelopoiesis associated with *Apoe* deficiency was also reduced in $SLc2a1^{+/-}$ mice. In our study, homozygous deletion of GLUT1 did not alter blood cell counts, therefore suggesting that their findings may only be applicable in the setting of the *ApoE*-null background or, alternatively, that homozygous, rather than heterozygous, deficiency has differential effects on myeloid biology. Single or double mutation may regulate the extent of MΦ activation, which may provide insight into inhibition of GLUT1 function pharmacologically.

Finally, to further probe how GLUT1-mediated MΦ metabolism may have affected atheroma biology, we considered that glucose is essential in maintaining functional MΦ phagocytic capacity. Venter et al. (60) demonstrated that glycolysis fuels LPS-induced MΦ cell shape changes and phagocytosis of zymosan particles in the RAW MΦ 246.7 cell line. Additionally, besides its important role in glycolysis, 6-phosphofructo-2-kinase/fructose-2, 6-biphosphatase 3 (PFKFB3) regulates actin cytoskeleton remodeling (122). Nishizawa et al. (121) showed that knocking down GLUT1 through siRNA decreased PFKFB3 gene expression, a finding which our gene expression, metabolomic, and bioenergetic analysis supports. Therefore, we speculated that the lack of GLUT1 may alter actin cytoskeleton remodeling in MΦs. MΦs with reduced ability to rearrange actin cannot form proper pseudopodia, and therefore phagocytic capacity is impaired (123). MΦs are necessary for homeostatic turnover and removal of dead or dying cells during pathologic states, a type of phagocytosis known as efferocytosis, which is crucial in both adipose tissue and atherosclerotic lesions (124). Insufficient clearance of dead cells can lead to proinflammatory MΦ activation and damage to surrounding tissue (125). For example, unabated engulfment of oxLDL renders MΦs susceptible to apoptosis, allowing non-cleared apoptotic cells to succumb to secondary necrosis and release cellular material into the microenvironment and ultimately exacerbate tissue damage (118, 126). If MΦs were able to effectively clear apoptotic bodies, the extent of continued inflammation and/or secondary necrosis would be reduced (60, 125, 127). Therefore, to characterize the effect of GLUT1 on phagocytic capacity, we performed an ex vivo assay to test the capacity of MΦs to bind and phagocytose opsonized microspheres. Critically, $Slc2a1^{M-/-}$ MΦs showed no defect in binding beads yet displayed a significant defect in capacity to engulf beads. Thus, reduced GLUT1-associated phagocytic capacity may explain increased necrotic content in lesions of $Slc2a1^{M-/-}$ mice.

In conclusion, disruption of MΦ glycolysis and PPP through GLUT1 deletion prevented normal MΦ metabolic and immune function in tissue homeostasis, shifting adipose tissue MΦs toward a moderately alternative phenotype, delaying hyperglycemia in obesity, and exacerbating necrotic core formation in atherosclerotic lesions. Therefore, we report a role for myeloid-specific GLUT1-mediated glucose metabolism in directing MΦ inflammatory potential in metabolic disease. However, the fact that the phenotype was not more dramatic speaks to the metabolic flexibility of MΦs. These studies identify a critical role in MΦ function for GLUT1-dependent glucose transport and metabolism coupled to maintenance of proper tissue homeostatic responses.

References

1. Cozzo, A. J., A. M. Fuller, and L. Makowski. 2017. Contribution of adipose tissue to development of cancer. *Compr. Physiol.* 8: 237–282.
2. Kelly, B., and L. A. O'Neill. 2015. Metabolic reprogramming in macrophages and dendritic cells in innate immunity. *Cell Res.* 25: 771–784.
3. O'Neill, L. A., and E. J. Pearce. 2016. Immunometabolism governs dendritic cell and macrophage function. *J. Exp. Med.* 213: 15–23.
4. Kratz, M., B. R. Coats, K. B. Hisert, D. Hagman, V. Mutskov, E. Peris, K. Q. Schoenfelt, J. N. Kuzma, I. Larson, P. S. Billing, et al. 2014. Metabolic dysfunction drives a mechanistically distinct proinflammatory phenotype in adipose tissue macrophages. *Cell Metab.* 20: 614–625.
5. Xu, X., A. Grijalva, A. Skowronski, M. van Eijk, M. J. Serlie, and A. W. Ferrante, Jr. 2013. Obesity activates a program of lysosomal-dependent lipid metabolism in adipose tissue macrophages independently of classic activation. *Cell Metab.* 18: 816–830.
6. Huang, S. C., B. Everts, Y. Ivanova, D. O'Sullivan, M. Nascimento, A. M. Smith, W. Beatty, L. Love-Gregory, W. Y. Lam, C. M. O'Neill, et al. 2014. Cell-intrinsic lysosomal lipolysis is essential for alternative activation of macrophages. *Nat. Immunol.* 15: 846–855.
7. Cader, M. Z., K. Boroviak, Q. Zhang, G. Assadi, S. L. Kempster, G. W. Sewell, S. Saveljeva, J. W. Ashcroft, S. Clare, S. Mukhopadhyay, et al. 2016. C13orf31 (FAMIN) is a central regulator of immunometabolic function. *Nat. Immunol.* 17: 1046–1056.
8. Olenchock, B. A., J. C. Rathmell, and M. G. Vander Heiden. 2017. Biochemical underpinnings of immune cell metabolic phenotypes. *Immunity* 46: 703–713.
9. Van den Bossche, J., L. A. O'Neill, and D. Menon. 2017. Macrophage immunometabolism: where are we (going)? *Trends Immunol.* 38: 395–406.
10. Ryan, D. G., and L. A. J. O'Neill. 2017. Krebs cycle rewired for macrophage and dendritic cell effector functions. *FEBS Lett.* 591: 2992–3006.
11. Freemerman, A. J., A. R. Johnson, G. N. Sacks, J. J. Milner, E. L. Kirk, M. A. Troester, A. N. Macintyre, P. Goraksha-Hicks, J. C. Rathmell, and L. Makowski. 2014. Metabolic reprogramming of macrophages: glucose transporter 1 (GLUT1)-mediated glucose metabolism drives a proinflammatory phenotype. *J. Biol. Chem.* 289: 7884–7896.
12. Tannahill, G. M., A. M. Curtis, J. Adamik, E. M. Palsson-McDermott, A. F. McGettrick, G. Goel, C. Frezza, N. J. Bernard, B. Kelly, N. H. Foley, et al. 2013. Succinate is an inflammatory signal that induces IL-1β through HIF-1α. *Nature* 496: 238–242.
13. Vats, D., L. Mukundan, J. I. Odegaard, L. Zhang, K. L. Smith, C. R. Morel, R. A. Wagner, D. R. Greaves, P. J. Murray, and A. Chawla. 2006. Oxidative metabolism and PGC-1beta attenuate macrophage-mediated inflammation. [Published erratum appears in 2006 *Cell Metab.* 4: 255.] *Cell Metab.* 4: 13–24.
14. Odegaard, J. I., R. R. Ricardo-Gonzalez, M. H. Goforth, C. R. Morel, V. Subramanian, L. Mukundan, A. Red Eagle, D. Vats, F. Brombacher, A. W. Ferrante, and A. Chawla. 2007. Macrophage-specific PPARgamma controls alternative activation and improves insulin resistance. *Nature* 447: 1116–1120.
15. Newsholme, P., R. Curi, S. Gordon, and E. A. Newsholme. 1986. Metabolism of glucose, glutamine, long-chain fatty acids and ketone bodies by murine macrophages. *Biochem. J.* 239: 121–125.
16. Salh, B., R. Wagey, A. Marotta, J. S. Tao, and S. Pelech. 1998. Activation of phosphatidylinositol 3-kinase, protein kinase B, and p70 S6 kinases in lipopolysaccharide-stimulated raw 264.7 cells: differential effects of rapamycin, Ly294002, and wortmannin on nitric oxide production. *J. Immunol.* 161: 6947–6954.
17. Spolarics, Z., and J. X. Wu. 1997. Tumor necrosis factor alpha augments the expression of glucose-6-phosphate dehydrogenase in rat hepatic endothelial and Kupffer cells. *Life Sci.* 60: 565–571.
18. Aouadi, M., P. Vangala, J. C. Yawe, M. Tencerova, S. M. Nicoloro, J. L. Cohen, Y. Shen, and M. P. Czech. 2014. Lipid storage by adipose tissue macrophages regulates systemic glucose tolerance. *Am. J. Physiol. Endocrinol. Metab.* 307: E374–E383.
19. Johnson, A. R., J. J. Milner, and L. Makowski. 2012. The inflammation highway: metabolism accelerates inflammatory traffic in obesity. *Immunol. Rev.* 249: 218–238.
20. Johnson, A. R., Y. Qin, A. J. Cozzo, A. J. Freemerman, M. J. Huang, L. Zhao, B. P. Sampey, J. J. Milner, M. A. Beck, B. Damania, et al. 2016. Metabolic reprogramming through fatty acid transport protein 1 (FATP1) regulates macrophage inflammatory potential and adipose inflammation. *Mol. Metab.* 5: 506–526.
21. Van den Bossche, J., J. Baardman, N. A. Otto, S. van der Velden, A. E. Neele, S. M. van den Berg, R. Luque-Martin, H. J. Chen, M. C. Boshuizen, M. Ahmed, et al. 2016. Mitochondrial dysfunction prevents repolarization of inflammatory macrophages. *Cell Rep.* 17: 684–696.
22. Huang, S. C., A. M. Smith, B. Everts, M. Colonna, E. L. Pearce, J. D. Schilling, and E. J. Pearce. 2016. Metabolic reprogramming mediated by the mTORC2-IRF4 signaling Axis is essential for macrophage alternative activation. *Immunity* 45: 817–830.

23. Tan, Z., N. Xie, H. Cui, D. R. Moellering, E. Abraham, V. J. Thannickal, and G. Liu. 2015. Pyruvate dehydrogenase kinase 1 participates in macrophage polarization via regulating glucose metabolism. *J. Immunol.* 194: 6082–6089.

24. Covarrubias, A. J., H. I. Aksoylar, J. Yu, N. W. Snyder, A. J. Worth, S. S. Iyer, J. Wang, I. Ben-Sahra, V. Byles, T. Polynne-Stapornkul, et al. 2016. Akt-mTORC1 signaling regulates Acly to integrate metabolic input to control of macrophage activation. *Elife.* DOI: 10.7554/eLife.11612.

25. Langston, P. K., M. Shibata, and T. Horng. 2017. Metabolism supports macrophage activation. *Front. Immunol.* 8: 61.

26. Geeraerts, X., E. Bolli, S. M. Fendt, and J. A. Van Ginderachter. 2017. Macrophage metabolism as therapeutic target for cancer, atherosclerosis, and obesity. *Front. Immunol.* 8: 289.

27. Iwaki, T., T. Urano, and K. Umemura. 2012. PAI-1, progress in understanding the clinical problem and its aetiology. *Br. J. Haematol.* 157: 291–298.

28. Weisberg, S. P., D. McCann, M. Desai, M. Rosenbaum, R. L. Leibel, and A. W. Ferrante, Jr. 2003. Obesity is associated with macrophage accumulation in adipose tissue. *J. Clin. Invest.* 112: 1796–1808.

29. Sundaram, S., A. R. Johnson, and L. Makowski. 2013. Obesity, metabolism and the microenvironment: links to cancer. *J. Carcinog.* 12: 19.

30. Lumeng, C. N., I. Maillard, and A. R. Saltiel. 2009. T-ing up inflammation in fat. *Nat. Med.* 15: 846–847.

31. Xu, H., G. T. Barnes, Q. Yang, G. Tan, D. Yang, C. J. Chou, J. Sole, A. Nichols, J. S. Ross, L. A. Tartaglia, and H. Chen. 2003. Chronic inflammation in fat plays a crucial role in the development of obesity-related insulin resistance. *J. Clin. Invest.* 112: 1821–1830.

32. Tabas, I., G. García-Cardeña, and G. K. Owens. 2015. Recent insights into the cellular biology of atherosclerosis. *J. Cell Biol.* 209: 13–22.

33. Schaftenaar, F., V. Frodermann, J. Kuiper, and E. Lutgens. 2016. Atherosclerosis: the interplay between lipids and immune cells. *Curr. Opin. Lipidol.* 27: 209–215.

34. Young, C. D., A. S. Lewis, M. C. Rudolph, M. D. Ruehle, M. R. Jackman, U. J. Yun, O. Ilkun, R. Pereira, E. D. Abel, and S. M. Anderson. 2011. Modulation of glucose transporter 1 (GLUT1) expression levels alters mouse mammary tumor cell growth in vitro and in vivo. *PLoS One* 6: e23205.

35. Makowski, L., K. C. Brittingham, J. M. Reynolds, J. Suttles, and G. S. Hotamisligil. 2005. The fatty acid-binding protein, aP2, coordinates macrophage cholesterol trafficking and inflammatory activity. Macrophage expression of aP2 impacts peroxisome proliferator-activated receptor gamma and IkappaB kinase activities. *J. Biol. Chem.* 280: 12888–12895.

36. Grevengoed, T. J., D. E. Cooper, P. A. Young, J. M. Ellis, and R. A. Coleman. 2015. Loss of long-chain acyl-CoA synthetase isoform 1 impairs cardiac autophagy and mitochondrial structure through mechanistic target of rapamycin complex 1 activation. *FASEB J.* 29: 4641–4653.

37. Bhatt, A. P., S. R. Jacobs, A. J. Freemerman, L. Makowski, J. C. Rathmell, D. P. Dittmer, and B. Damania. 2012. Dysregulation of fatty acid synthesis and glycolysis in non-Hodgkin lymphoma. *Proc. Natl. Acad. Sci. USA* 109: 11818–11823.

38. Van den Bossche, J., J. Baardman, and M. P. de Winther. 2015. Metabolic characterization of polarized M1 and M2 bone marrow-derived macrophages using real-time extracellular flux analysis. *J. Vis. Exp.* DOI: 10.3791/53424.

39. Liu, X., S. Sadhukhan, S. Sun, G. R. Wagner, M. D. Hirschey, L. Qi, H. Lin, and J. W. Locasale. 2015. High-resolution metabolomics with acyl-CoA profiling reveals widespread remodeling in response to diet. *Mol. Cell. Proteomics* 14: 1489–1500.

40. Liu, X., Z. Ser, and J. W. Locasale. 2014. Development and quantitative evaluation of a high-resolution metabolomics technology. *Anal. Chem.* 86: 2175–2184.

41. Qin, Y., J. L. Hamilton, M. D. Bird, M. M. Chen, L. Ramirez, A. Zahs, E. J. Kovacs, and L. Makowski. 2014. Adipose inflammation and macrophage infiltration after binge ethanol and burn injury. *Alcohol. Clin. Exp. Res.* 38: 204–213.

42. Zhao, L., A. J. Cozzo, A. R. Johnson, T. Christensen, A. J. Freemerman, J. E. Bear, J. D. Rotty, B. J. Bennett, and L. Makowski. 2017. Lack of myeloid Fatp1 increases atherosclerotic lesion size in Ldlr$^{-/-}$ mice. *Atherosclerosis* 266: 182–189.

43. Johnson, A. R., M. D. Wilkerson, B. P. Sampey, M. A. Troester, D. N. Hayes, and L. Makowski. 2016. Cafeteria diet-induced obesity causes oxidative damage in white adipose. *Biochem. Biophys. Res. Commun.* 473: 545–550.

44. Sundaram, S., T. L. Le, L. Essaid, A. J. Freemerman, M. J. Huang, J. A. Galanko, K. K. McNaughton, K. M. Bendt, D. B. Darr, M. A. Troester, and L. Makowski. 2014. Weight loss reversed obesity-induced HGF/c-Met pathway and basal-like breast cancer progression. *Front. Oncol.* 4: 175.

45. Sundaram, S., A. J. Freemerman, A. R. Johnson, J. J. Milner, K. K. McNaughton, J. A. Galanko, K. M. Bendt, D. B. Darr, C. M. Perou, M. A. Troester, and L. Makowski. 2013. Role of HGF in obesity-associated tumorigenesis: C3(1)-TAg mice as a model for human basal-like breast cancer. *Breast Cancer Res. Treat.* 142: 489–503.

46. Sundaram, S., A. J. Freemerman, J. A. Galanko, K. K. McNaughton, K. M. Bendt, D. B. Darr, M. A. Troester, and L. Makowski. 2014. Obesity-mediated regulation of HGF/c-Met is associated with reduced basal-like breast cancer latency in parous mice. *PLoS One* 9: e111394.

47. Björkbacka, H., V. V. Kunjathoor, K. J. Moore, S. Koehn, C. M. Ordija, M. A. Lee, T. Means, K. Halmen, A. D. Luster, D. T. Golenbock, and M. W. Freeman. 2004. Reduced atherosclerosis in MyD88-null mice links elevated serum cholesterol levels to activation of innate immunity signaling pathways. *Nat. Med.* 10: 416–421.

48. Rotllan, N., A. C. Wanschel, A. Fernández-Hernando, A. G. Salerno, S. Offermanns, W. C. Sessa, and C. Fernández-Hernando. 2015. Genetic evidence supports a major role for Akt1 in VSMCs during atherogenesis. *Circ. Res.* 116: 1744–1752.

49. DeLoid, G. M., T. H. Sulahian, A. Imrich, and L. Kobzik. 2009. Heterogeneity in macrophage phagocytosis of *Staphylococcus aureus* strains: high-throughput scanning cytometry-based analysis. *PLoS One* 4: e6209.

50. Pike Winer, L. S., and M. Wu. 2014. Rapid analysis of glycolytic and oxidative substrate flux of cancer cells in a microplate. *PLoS One* 9: e109916.

51. Brand, M. D., and D. G. Nicholls. 2011. Assessing mitochondrial dysfunction in cells. *Biochem. J.* 435: 297–312.

52. Infantino, V., V. Iacobazzi, F. Palmieri, and A. Menga. 2013. ATP-citrate lyase is essential for macrophage inflammatory response. *Biochem. Biophys. Res. Commun.* 440: 105–111.

53. Wei, X., H. Song, L. Yin, M. G. Rizzo, R. Sidhu, D. F. Covey, D. S. Ory, and C. F. Semenkovich. 2016. Fatty acid synthesis configures the plasma membrane for inflammation in diabetes. *Nature* 539: 294–298.

54. Michalek, R. D., V. A. Gerriets, S. R. Jacobs, A. N. Macintyre, N. J. MacIver, E. F. Mason, S. A. Sullivan, A. G. Nichols, and J. C. Rathmell. 2011. Cutting edge: distinct glycolytic and lipid oxidative metabolic programs are essential for effector and regulatory CD4+ T cell subsets. *J. Immunol.* 186: 3299–3303.

55. Maciver, N. J., S. R. Jacobs, H. L. Wieman, J. A. Wofford, J. L. Coloff, and J. C. Rathmell. 2008. Glucose metabolism in lymphocytes is a regulated process with significant effects on immune cell function and survival. *J. Leukoc. Biol.* 84: 949–957.

56. McKenna, S., B. Butler, L. Jatana, S. Ghosh, and C. J. Wright. 2017. Inhibition of IκBβ/NFκB signaling prevents LPS-induced IL1β expression without increasing apoptosis in the developing mouse lung. *Pediatr. Res.* 82: 1064–1072.

57. Dos Santos, L. M., T. M. da Silva, J. H. Azambuja, P. T. Ramos, P. S. Oliveira, E. F. da Silveira, N. S. Pedra, K. Galdino, C. A. do Couto, M. S. Soares, et al. 2017. Methionine and methionine sulfoxide treatment induces M1/classical macrophage polarization and modulates oxidative stress and purinergic signaling parameters. *Mol. Cell. Biochem.* 424: 69–78.

58. Subramanian, S., C. Y. Han, T. Chiba, T. S. McMillen, S. A. Wang, A. Haw, III, E. A. Kirk, K. D. O'Brien, and A. Chait. 2008. Dietary cholesterol worsens adipose tissue macrophage accumulation and atherosclerosis in obese LDL receptor-deficient mice. *Arterioscler. Thromb. Vasc. Biol.* 28: 685–691.

59. Poon, I. K., C. D. Lucas, A. G. Rossi, and K. S. Ravichandran. 2014. Apoptotic cell clearance: basic biology and therapeutic potential. *Nat. Rev. Immunol.* 14: 166–180.

60. Venter, G., F. T. Oerlemans, M. Wijers, M. Willemse, J. A. Fransen, and B. Wieringa. 2014. Glucose controls morphodynamics of LPS-stimulated macrophages. *PLoS One* 9: e96786.

61. Schrijvers, D. M., G. R. De Meyer, A. G. Herman, and W. Martinet. 2007. Phagocytosis in atherosclerosis: molecular mechanisms and implications for plaque progression and stability. *Cardiovasc. Res.* 73: 470–480.

62. Thiele, L., J. E. Diederichs, R. Reszka, H. P. Merkle, and E. Walter. 2003. Competitive adsorption of serum proteins at microparticles affects phagocytosis by dendritic cells. *Biomaterials* 24: 1409–1418.

63. Wong, S. Y., L. M. Guerdoud, A. Cantin, and D. P. Speert. 1999. Glucose stimulates phagocytosis of unopsonized *Pseudomonas aeruginosa* by cultivated human alveolar macrophages. *Infect. Immun.* 67: 16–21.

64. Champion, J. A., A. Walker, and S. Mitragotri. 2008. Role of particle size in phagocytosis of polymeric microspheres. *Pharm. Res.* 25: 1815–1821.

65. MacIver, N. J., and J. C. Rathmell. 2017. Editorial overview: metabolism of T cells: integrating nutrients, signals, and cell fate. *Curr. Opin. Immunol.* 46: viii–xi.

66. Mah, A. Y., A. Rashidi, M. P. Keppel, N. Saucier, E. K. Moore, J. B. Alinger, S. K. Tripathy, S. K. Agarwal, E. K. Jeng, H. C. Wong, et al. 2017. Glycolytic requirement for NK cell cytotoxicity and cytomegalovirus control. *JCI Insight.* DOI: 10.1172/jci.insight.95128.

67. Johnson, M. O., M. M. Wolf, M. Z. Madden, G. Andrejeva, A. Sugiura, D. C. Contreras, D. Maseda, M. V. Liberti, K. Paz, R. J. Kishton, et al. 2018. Distinct regulation of Th17 and Th1 cell differentiation by glutaminase-dependent metabolism. *Cell.* DOI: 10.1016/j.cell.2018.10.001.

68. 2010. Researchers find obesity negatively affects results of HAART treatment. *AIDS Policy Law* 25: 1.

69. Siska, P. J., G. J. van der Windt, R. J. Kishton, S. Cohen, W. Eisner, N. J. MacIver, A. P. Kater, J. B. Weinberg, and J. C. Rathmell. 2016. Suppression of Glut1 and glucose metabolism by decreased Akt/mTORC1 signaling drives T cell impairment in B cell leukemia. *J. Immunol.* 197: 2532–2540.

70. Gerriets, V. A., R. J. Kishton, M. O. Johnson, S. Cohen, P. J. Siska, A. G. Nichols, M. O. Warmoes, A. A. de Cubas, N. J. MacIver, J. W. Locasale, et al. 2016. Foxp3 and Toll-like receptor signaling balance T$_{reg}$ cell anabolic metabolism for suppression. *Nat. Immunol.* 17: 1459–1466.

71. Saucillo, D. C., V. A. Gerriets, J. Sheng, J. C. Rathmell, and N. J. Maciver. 2014. Leptin metabolically licenses T cells for activation to link nutrition and immunity. *J. Immunol.* 192: 136–144.

72. Liu, T., R. J. Kishton, A. N. Macintyre, V. A. Gerriets, H. Xiang, X. Liu, E. D. Abel, D. Rizzieri, J. W. Locasale, and J. C. Rathmell. 2014. Glucose transporter 1-mediated glucose uptake is limiting for B-cell acute lymphoblastic leukemia anabolic metabolism and resistance to apoptosis. [Published erratum appears in 2014 *Cell Death Dis.* 5: e1516.] *Cell Death Dis.* 5: e1470.

73. Ortega, R. A., W. Barham, K. Sharman, O. Tikhomirov, T. D. Giorgio, and F. E. Yull. 2016. Manipulating the NF-κB pathway in macrophages using mannosylated, siRNA-delivering nanoparticles can induce immunostimulatory and tumor cytotoxic functions. *Int. J. Nanomedicine* 11: 2163–2177.

74. Duivenvoorden, R., J. Tang, D. P. Cormode, A. J. Mieszawska, D. Izquierdo-Garcia, C. Ozcan, M. J. Otten, N. Zaidi, M. E. Lobatto, S. M. van Rijs, et al. 2014. A statin-loaded reconstituted high-density lipoprotein nanoparticle inhibits atherosclerotic plaque inflammation. [Published erratum appears in 2014 *Nat. Commun.* 5: 3531.] *Nat. Commun.* 5: 3065.

75. Zhu, S., M. Niu, H. O'Mary, and Z. Cui. 2013. Targeting of tumor-associated macrophages made possible by PEG-sheddable, mannose-modified nanoparticles. *Mol. Pharm.* 10: 3525–3530.

76. Aouadi, M., M. Tencerova, P. Vangala, J. C. Yawe, S. M. Nicoloro, S. U. Amano, J. L. Cohen, and M. P. Czech. 2013. Gene silencing in adipose tissue macrophages regulates whole-body metabolism in obese mice. *Proc. Natl. Acad. Sci. USA* 110: 8278–8283.

77. Bonvini, A., A. Y. Coqueiro, J. Tirapegui, P. C. Calder, and M. M. Rogero. 2018. Immunomodulatory role of branched-chain amino acids. *Nutr. Rev.* 76: 840–856.

78. Jha, A. K., S. C. Huang, A. Sergushichev, V. Lampropoulou, Y. Ivanova, E. Loginicheva, K. Chmielewski, K. M. Stewart, J. Ashall, B. Everts, et al. 2015. Network integration of parallel metabolic and transcriptional data reveals metabolic modules that regulate macrophage polarization. *Immunity* 42: 419–430.

79. Mills, E. L., B. Kelly, A. Logan, A. S. Costa, M. Varma, C. E. Bryant, P. Tourlomousis, J. H. Dabritz, E. Gottlieb, I. Latorre, et al. 2016. Succinate dehydrogenase supports metabolic repurposing of mitochondria to drive inflammatory macrophages. *Cell.* 167: 457–470.e13.

80. Cordes, T., M. Wallace, A. Michelucci, A. S. Divakaruni, S. C. Sapcariu, C. Sousa, H. Koseki, P. Cabrales, A. N. Murphy, K. Hiller, and C. M. Metallo. 2016. Immunoresponsive gene 1 and itaconate inhibit succinate dehydrogenase to modulate intracellular succinate levels. *J. Biol. Chem.* 291: 14274–14284.

81. Lampropoulou, V., A. Sergushichev, M. Bambouskova, S. Nair, E. E. Vincent, E. Loginicheva, L. Cervantes-Barragan, X. Ma, S. C. Huang, T. Griss, et al. 2016. Itaconate links inhibition of succinate dehydrogenase with macrophage metabolic remodeling and regulation of inflammation. *Cell Metab.* 24: 158–166.

82. Van den Bossche, J., W. H. Lamers, E. S. Koehler, J. M. Geuns, L. Alhonen, A. Uimari, S. Pirnes-Karhu, E. Van Overmeire, Y. Morias, L. Brys, et al. 2012. Pivotal advance: arginase-1-independent polyamine production stimulates the expression of IL-4-induced alternatively activated macrophage markers while inhibiting LPS-induced expression of inflammatory genes. *J. Leukoc. Biol.* 91: 685–699.

83. Gobert, A. P., and K. T. Wilson. 2012. Editorial: orchestration of macrophage polarization by polyamines. *J. Leukoc. Biol.* 91: 677–679.

84. Baardman, J., I. Licht, M. P. de Winther, and J. Van den Bossche. 2015. Metabolic-epigenetic crosstalk in macrophage activation. *Epigenomics* 7: 1155–1164.

85. Szabó, C., G. J. Southan, E. Wood, C. Thiemermann, and J. R. Vane. 1994. Inhibition by spermine of the induction of nitric oxide synthase in J774.2 macrophages: requirement of a serum factor. *Br. J. Pharmacol.* 112: 355–356.

86. Van den Bossche, J., P. Bogaert, J. van Hengel, C. J. Guérin, G. Berx, K. Movahedi, R. Van den Bergh, A. Pereira-Fernandes, J. M. Geuns, H. Pircher, et al. 2009. Alternatively activated macrophages engage in homotypic and heterotypic interactions through IL-4 and polyamine-induced E-cadherin/catenin complexes. *Blood* 114: 4664–4674.

87. Suh, J. H., R. Y. Kim, and D. S. Lee. 2012. A new metabolomic assay to examine inflammation and redox pathways following LPS challenge. *J. Inflamm. (Lond.)* 9: 37.

88. Barilli, A., B. M. Rotoli, R. Visigalli, F. Ingoglia, M. Cirlini, B. Prandi, and V. Dall'Asta. 2015. Gliadin-mediated production of polyamines by RAW264.7 macrophages modulates intestinal epithelial permeability in vitro. *Biochim. Biophys. Acta* 1852: 1779–1786.

89. Wen, H., J. P. Ting, and L. A. O'Neill. 2012. A role for the NLRP3 inflammasome in metabolic diseases--did Warburg miss inflammation? *Nat. Immunol.* 13: 352–357.

90. Wen, H., D. Gris, Y. Lei, S. Jha, L. Zhang, M. T. Huang, W. J. Brickey, and J. P. Ting. 2011. Fatty acid-induced NLRP3-ASC inflammasome activation interferes with insulin signaling. *Nat. Immunol.* 12: 408–415.

91. Wang, I. M., H. Lin, S. J. Goldman, and M. Kobayashi. 2004. STAT-1 is activated by IL-4 and IL-13 in multiple cell types. *Mol. Immunol.* 41: 873–884.

92. Haschemi, A., P. Kosma, L. Gille, C. R. Evans, C. F. Burant, P. Starkl, B. Knapp, R. Haas, J. A. Schmid, C. Jandl, et al. 2012. The sedoheptulose kinase CARKL directs macrophage polarization through control of glucose metabolism. *Cell Metab.* 15: 813–826.

93. Morris, P. G., C. A. Hudis, D. Giri, M. Morrow, D. J. Falcone, X. K. Zhou, B. Du, E. Brogi, C. B. Crawford, L. Kopelovich, et al. 2011. Inflammation and increased aromatase expression occur in the breast tissue of obese women with breast cancer. *Cancer Prev. Res. (Phila.)* 4: 1021–1029.

94. Subbaramaiah, K., L. R. Howe, P. Bhardwaj, B. Du, C. Gravaghi, R. K. Yantiss, X. K. Zhou, V. A. Blaho, T. Hla, P. Yang, et al. 2011. Obesity is associated with inflammation and elevated aromatase expression in the mouse mammary gland. *Cancer Prev. Res. (Phila.)* 4: 329–346.

95. Sampey, B. P., A. J. Freemerman, J. Zhang, P. F. Kuan, J. A. Galanko, T. M. O'Connell, O. R. Ilkayeva, M. J. Muehlbauer, R. D. Stevens, C. B. Newgard, et al. 2012. Metabolomic profiling reveals mitochondrial-derived lipid biomarkers that drive obesity-associated inflammation. *PLoS One* 7: e38812.

96. Sampey, B. P., A. M. Vanhoose, H. M. Winfield, A. J. Freemerman, M. J. Muehlbauer, P. T. Fueger, C. B. Newgard, and L. Makowski. 2011. Cafeteria diet is a robust model of human metabolic syndrome with liver and adipose inflammation: comparison to high-fat diet. *Obesity (Silver Spring)* 19: 1109–1117.

97. Sun, X., P. Casbas-Hernandez, C. Bigelow, L. Makowski, D. Joseph Jerry, S. Smith Schneider, and M. A. Troester. 2012. Normal breast tissue of obese women is enriched for macrophage markers and macrophage-associated gene expression. *Breast Cancer Res. Treat.* 131: 1003–1012.

98. Subbaramaiah, K., P. G. Morris, X. K. Zhou, M. Morrow, B. Du, D. Giri, L. Kopelovich, C. A. Hudis, and A. J. Dannenberg. 2012. Increased levels of COX-2 and prostaglandin E2 contribute to elevated aromatase expression in inflamed breast tissue of obese women. *Cancer Discov.* 2: 356–365.

99. Lumeng, C. N., J. L. Bodzin, and A. R. Saltiel. 2007. Obesity induces a phenotypic switch in adipose tissue macrophage polarization. *J. Clin. Invest.* 117: 175–184.

100. Fujisaka, S., I. Usui, A. Bukhari, M. Ikutani, T. Oya, Y. Kanatani, K. Tsuneyama, Y. Nagai, K. Takatsu, M. Urakaze, et al. 2009. Regulatory mechanisms for adipose tissue M1 and M2 macrophages in diet-induced obese mice. *Diabetes* 58: 2574–2582.

101. Shaul, M. E., G. Bennett, K. J. Strissel, A. S. Greenberg, and M. S. Obin. 2010. Dynamic, M2-like remodeling phenotypes of CD11c+ adipose tissue macrophages during high-fat diet--induced obesity in mice. *Diabetes* 59: 1171–1181.

102. Zeyda, M., D. Farmer, J. Todoric, O. Aszmann, M. Speiser, G. Györi, G. J. Zlabinger, and T. M. Stulnig. 2007. Human adipose tissue macrophages are of an anti-inflammatory phenotype but capable of excessive pro-inflammatory mediator production. *Int. J. Obes.* 31: 1420–1428.

103. Li, P., M. Lu, M. T. Nguyen, E. J. Bae, J. Chapman, D. Feng, M. Hawkins, J. E. Pessin, D. D. Sears, A. K. Nguyen, et al. 2010. Functional heterogeneity of CD11c-positive adipose tissue macrophages in diet-induced obese mice. *J. Biol. Chem.* 285: 15333–15345.

104. Wentworth, J. M., G. Naselli, W. A. Brown, L. Doyle, B. Phipson, G. K. Smyth, M. Wabitsch, P. E. O'Brien, and L. C. Harrison. 2010. Pro-inflammatory CD11c+CD206+ adipose tissue macrophages are associated with insulin resistance in human obesity. *Diabetes* 59: 1648–1656.

105. Nakajima, S., V. Koh, L. F. Kua, J. So, L. Davide, K. S. Lim, S. H. Petersen, W. P. Yong, A. Shabbir, and K. Kono. 2016. Accumulation of CD11c+CD163+ adipose tissue macrophages through upregulation of intracellular 11β-HSD1 in human obesity. *J. Immunol.* 197: 3735–3745.

106. Zheng, C., Q. Yang, J. Cao, N. Xie, K. Liu, P. Shou, F. Qian, Y. Wang, and Y. Shi. 2016. Local proliferation initiates macrophage accumulation in adipose tissue during obesity. *Cell Death Dis.* 7: e2167.

107. Hopkins, P. N. 2013. Molecular biology of atherosclerosis. *Physiol. Rev.* 93: 1317–1542.

108. Shirai, T., R. R. Nazarewicz, B. B. Wallis, R. E. Yanes, R. Watanabe, M. Hilhorst, L. Tian, D. G. Harrison, J. C. Giacomini, T. L. Assimes, et al. 2016. The glycolytic enzyme PKM2 bridges metabolic and inflammatory dysfunction in coronary artery disease. *J. Exp. Med.* 213: 337–354.

109. Erbay, E., V. R. Babaev, J. R. Mayers, L. Makowski, K. N. Charles, M. E. Snitow, S. Fazio, M. M. Wiest, S. M. Watkins, M. F. Linton, and G. S. Hotamisligil. 2009. Reducing endoplasmic reticulum stress through a macrophage lipid chaperone alleviates atherosclerosis. [Published erratum appears in 2010 *Nat. Med.* 16: 237.] *Nat. Med.* 15: 1383–1391.

110. Stöger, J. L., M. J. Gijbels, S. van der Velden, M. Manca, C. M. van der Loos, E. A. Biessen, M. J. Daemen, E. Lutgens, and M. P. de Winther. 2012. Distribution of macrophage polarization markers in human atherosclerosis. *Atherosclerosis* 225: 461–468.

111. Feig, J. E., J. X. Rong, R. Shamir, M. Sanson, Y. Vengrenyuk, J. Liu, K. Rayner, K. Moore, M. Garabedian, and E. A. Fisher. 2011. HDL promotes rapid atherosclerosis regression in mice and alters inflammatory properties of plaque monocyte-derived cells. [Published erratum appears in 2011 *Proc. Nat. Acad. Sci. USA.* 108: 14371.] *Proc. Natl. Acad. Sci. USA* 108: 7166–7171.

112. Feig, J. E., S. Parathath, J. X. Rong, S. L. Mick, Y. Vengrenyuk, L. Grauer, S. G. Young, and E. A. Fisher. 2011. Reversal of hyperlipidemia with a genetic switch favorably affects the content and inflammatory state of macrophages in atherosclerotic plaques. *Circulation* 123: 989–998.

113. Cardilo-Reis, L., S. Gruber, S. M. Schreier, M. Drechsler, N. Papac-Milicevic, C. Weber, O. Wagner, H. Stangl, O. Soehnlein, and C. J. Binder. 2012. Interleukin-13 protects from atherosclerosis and modulates plaque composition by skewing the macrophage phenotype. *EMBO Mol. Med.* 4: 1072–1086.

114. Hanna, R. N., I. Shaked, H. G. Hubbeling, J. A. Punt, R. Wu, E. Herrley, C. Zaugg, H. Pei, F. Geissmann, K. Ley, and C. C. Hedrick. 2012. NR4A1 (Nur77) deletion polarizes macrophages toward an inflammatory phenotype and increases atherosclerosis. *Circ. Res.* 110: 416–427.

115. Sharma, N., Y. Lu, G. Zhou, X. Liao, P. Kapil, P. Anand, G. H. Mahabeleshwar, J. S. Stamler, and M. K. Jain. 2012. Myeloid Krüppel-like factor 4 deficiency augments atherogenesis in ApoE−/− mice--brief report. *Arterioscler. Thromb. Vasc. Biol.* 32: 2836–2838.

116. Ouimet, M., H. N. Ediriweera, U. M. Gundra, F. J. Sheedy, B. Ramkhelawon, S. B. Hutchison, K. Rinehold, C. van Solingen, M. D. Fullerton, K. Cecchini, et al. 2015. MicroRNA-33-dependent regulation of macrophage metabolism directs immune cell polarization in atherosclerosis. *J. Clin. Invest.* 125: 4334–4348.

117. Sarrazy, V., M. Viaud, M. Westerterp, S. Ivanov, S. Giorgetti-Peraldi, R. Guinamard, E. L. Gautier, E. B. Thorp, D. C. De Vivo, and L. Yvan-Charvet. 2016. Disruption of Glut1 in hematopoietic stem cells prevents myelopoiesis and enhanced glucose flux in Atheromatous plaques of ApoE(−/−) mice. *Circ. Res.* 118: 1062–1077.

118. Moore, K. J., F. J. Sheedy, and E. A. Fisher. 2013. Macrophages in atherosclerosis: a dynamic balance. *Nat. Rev. Immunol.* 13: 709–721.

119. Stary, H. C., A. B. Chandler, R. E. Dinsmore, V. Fuster, S. Glagov, W. Insull, Jr., M. E. Rosenfeld, C. J. Schwartz, W. D. Wagner, and R. W. Wissler. 1995. A definition of advanced types of atherosclerotic lesions and a histological classification of atherosclerosis. A report from the Committee on Vascular Lesions of the Council on Arteriosclerosis, American Heart Association. *Arterioscler. Thromb. Vasc. Biol.* 15: 1512–1531.

120. Lusis, A. J. 2000. Atherosclerosis. *Nature* 407: 233–241.

121. Nishizawa, T., J. E. Kanter, F. Kramer, S. Barnhart, X. Shen, A. Vivekanandan-Giri, V. Z. Wall, J. Kowitz, S. Devaraj, K. D. O'Brien, et al. 2014. Testing the role of myeloid cell glucose flux in inflammation and atherosclerosis. *Cell Rep.* 7: 356–365.

122. De Bock, K., M. Georgiadou, S. Schoors, A. Kuchnio, B. W. Wong, A. R. Cantelmo, A. Quaegebeur, B. Ghesquière, S. Cauwenberghs, G. Eelen, et al. 2013. Role of PFKFB3-driven glycolysis in vessel sprouting. *Cell* 154: 651–663.

123. Coppolino, M. G., R. Dierckman, J. Loijens, R. F. Collins, M. Pouladi, J. Jongstra-Bilen, A. D. Schreiber, W. S. Trimble, R. Anderson, and S. Grinstein. 2002. Inhibition of phosphatidylinositol-4-phosphate 5-kinase Ialpha impairs localized actin remodeling and suppresses phagocytosis. *J. Biol. Chem.* 277: 43849–43857.

124. Flannagan, R. S., V. Jaumouillé, K. K. Huynh, J. D. Plumb, G. P. Downey, M. A. Valvano, and S. Grinstein. 2012. Burkholderia cenocepacia disrupts host cell actin cytoskeleton by inactivating Rac and Cdc42. *Cell. Microbiol.* 14: 239–254.

125. Boutens, L., and R. Stienstra. 2016. Adipose tissue macrophages: going off track during obesity. *Diabetologia* 59: 879–894.

126. Randolph, G. J. 2014. Mechanisms that regulate macrophage burden in atherosclerosis. *Circ. Res.* 114: 1757–1771.

127. Moore, K. J., and I. Tabas. 2011. Macrophages in the pathogenesis of atherosclerosis. *Cell* 145: 341–355.